Slovak University of Technology in Bratislava
Faculty of Electrical Engineering and
Information Technology

Ing. Martin Ziman

Dissertation Thesis Abstract

Advanced 3D photonic devices

to obtain the Academic Title of Philisophiae doctor (PhD.)

in the doctorate degree study programme*:* Electronics and Photonics
in the field of study: Electrotechnics
Form of Study: Full-time

Place and Date: Bratislava 5.6.2024

Dissertation Thesis has been prepared at the Institute of Electronics and Photonics, Faculty of Electrical Engineering and Information Technology, Slovak University of Technology in Bratislava.

Submitter: Ing. Martin Ziman
Institute of Electronics and Photonics
Faculty of Electrical Engineering and Information Technology
Slovak University of Technology in Bratislava
Ilkovičova 3, 81219 Bratislava

Supervisor: doc. Ing. Anton Kuzma, PhD.
Institute of Electronics and Photonics
Faculty of Electrical Engineering and Information Technology
Slovak University of Technology in Bratislava
Ilkovičova 3, 81219 Bratislava

Readers: prof. Mgr. Ivan Martinček, PhD.
Department of Physics
Faculty of Electrical Engineering and Information Technology
University of Žilina
Univerzitná 1, 010 26 Žilina

doc. Ing. Jozef Novák, DrSc.
Institute of Electrical Engineering
Slovak Academy of Sciences
Dúbravská cesta 9, 841 04 Bratislava

Dissertation Thesis Defense will be held on 5.6.2024 at 9:00 a.m.
at Faculty of Electrical Engineering and Information Technology, Slovak University of Technology in Bratislava, Ilkovičova 3, 81219 Bratislava

……………………………………..
Prof. Ing. Vladimír Kutiš, PhD.
Dean of FEI of STU
Ilkovičova 3, 812 19 Bratislava

Contents

Introduction

The integration of photonic devices on a single chip also poses a problem, as different material platforms excel in different functions of a supposed integrated chip. The mature CMOS processes are bound to silicon-based materials, which can be used for light propagation, modulation, and also photodetection (with the introduction of germanium). However, one essential function of photonics remains out of the domain of Si-based materials - light excitation. The approaches to overcome this shortcoming used today include the use of external sources with on-chip coupling elements (edge and grating couplers), as well as various forms of heterogeneous and hybrid integration. The product of heterogenous integration is similar to that of a functionally complete monolithically integrated chip. Hybrid integration aims to prepare the light generation die beforehand and bond it with the passive chip using wire bonds (more recently vertical vias [1]) in the packaging stage. The approaches mentioned above require a great deal of flexibility in various stages of PIC manufacturing using conventional top-down processes [2].

Novel polymeric materials show promise in terms of much-needed interconnections by enabling the use of additive fabrication techniques such as Direct Laser Writing (DLW) and stereolithography (SLA) [3]. The fibre-to-chip interconnects in the form of sockets and microlenses that can be directly fabricated on the fibre and chip edges are within the realm of possibilities unlocked by the novel additive fabrication techniques. This lends polymer-based photonic devices to various sensing applications using fibre probes and on-chip microfluidic structures [4, 5].

Combining photonic devices with plasmonic-based structures further aids in enhancing the capabilities of existing devices. The difference between the size and speed of photonic and electronic devices could also be bridged by plasmonics. Plasmonics deals with generating, transmitting, and processing signals at optical wavelengths using the physical characteristics of metallic surfaces and metallic nanoparticles. Plasmon-based couplers and electro-optic modulators provide an efficient way of signal conversion between the electric and photonic parts of a hybrid system. In addition, plasmonics has already been found to be applicable in biosensing and spectroscopy.

This work focuses on the design and optimisation of 3D polymer-based photonic devices for light coupling, splitting, and environmental sensing. The devices described in this work are made of IP-Dip photoresist and designed explicitly for DLW fabrication. The polymeric devices were prepared by the team at the University of Žilina. Further, the work elaborates on the possibility of integrating plasmonic structures into polymeric devices and SiON-based photonic devices for sensing applications.

Goals of the thesis

1. To obtain knowledge in the field of design of 3D photonic structures and photonic devices with the use of plasmonic effects for sensing, lab-on-fibre (lab-on-chip) purposes.

2. To determine the optimisation of 3D photonic structures based on polymer materials related to the existing technological limits and redefine the simulation models in terms of obtained characteristics.

3. To design 3D photonic devices using polymer material base such as power splitter or sensor.

4. To analyse the prepared structures using available methods such as optical power, spectroscopy or microscopy methods.

1 Design and Optimisation of a Power Splitter Based on a 3D MMI Coupler

Multi-mode interference (MMI) coupler offers an alternative solution to the typical directional coupler while maintaining output power balance, low loss, and high fabrication tolerance. The MMI coupler solidified its place in photonic integrated circuits (PICs) because of its versatility and favourable characteristics. The applications of MMI coupler cover a wide range, starting with basic power splitting [6–8], switching [9, 10], polarisation dividing [11], multiplexing [12, 13], sensing [14], and more recently it has even been used in PICs for machine learning [15].

Most MMI devices mentioned above were based on conventional semiconductor material platforms bound by the available fabrication methods. As a result, their design process has not changed significantly since the review published by Soldano and Pennings in 1995 [16].

The following section presents the design and optimisation of two MMI-based power splitters prepared using the DLW method. The subsequent simulation investigation of the deviations from the designed function of the structures is also presented.

1.1. Simulation Models

The base structure of an MMI coupler is a multi-mode waveguide that supports many propagating modes, usually with a single-mode waveguide at the input and an appropriate number of single-mode output waveguides at the end. The beam propagation method (BPM) is a suitable tool for simulating such devices because of the absence of abrupt changes in the direction of propagating light.

Conventional MMI couplers used for splitting comprise the input waveguide, the MMI section, and the output waveguides to outcouple the split signal. Factors limiting the design of an MMI include the refractive indices of the core materials (n_f) and the cladding materials (n_c) and the operational wavelength of the device (λ_0). In the material platform used, the values are $n_f = 1.53$ (Nanoscribe IP-Dip) [17] and $n_c = 1$ (air). The input light is the mode supported by a single-mode fibre (SMF) attached to the prepared MMI coupler. In the case of two output modes at the MMI output, the width should be ~18 µm (2 times the input mode field diameter), and in three, it should be ~27 µm. The characteristic beat length of the coupler (L_π) can be obtained from Equation (1.1), where W stands for the width of the MMI coupler [16].

$$L_\pi \approx \frac{4n_f W^2}{3\lambda_0} \tag{1.1}$$

Considering the design requirements and fabrication limitations, two MMI splitters were designed and fabricated, one with four interference maxima at the output (1×4 splitter) and one with nine interference maxima (1×9 splitter). Different simulation models were created for each MMI splitter, with power monitors throughout the structure (Fig. 1.1).
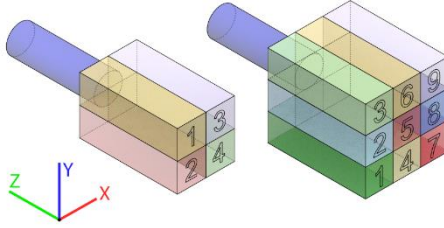
Fig. 1.1: Schematic of the layout of the BPM power monitor for each splitter model with four power monitors for 1×4 and nine monitors for 1×9 power splitter.

1.2. Simulations of Optimal Dimensions and Spectral Characteristics

First, the width of the MMI (W) was determined considering the design limitations. The widths of the couplers were 18 µm and 26 µm. The optimal beat length values were then simulated to be $L_\pi = 162$ µm in the case of the 1×4 splitter and $L_\pi = 225$ µm in the case of the 1×9 splitter. In the case of the 1×4 splitter, the outputs were symmetrical throughout the structure. In the 1×9 splitter, the interference distributes the power from the central monitor to the remaining ones.

To further verify the function of the MMI splitters, output modal field distributions (Fig. 1.2) were analysed at the end of the MMI. The interference images retain the shape of the input modal field, and the total insertion losses for all outputs do not exceed -0.75 dB for both designed couplers.
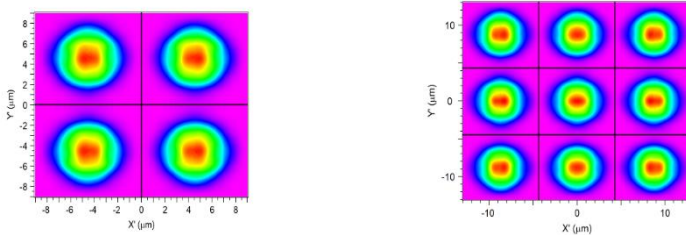

Fig. 1.2: Output modal field distribution at the end of the MMI splitters: 1×4 MMI (left); 1×9 MMI (right).

For a more complex analysis, the spectral characteristics of the splitters (Fig. 1.3) were simulated. These characteristics show that both splitters fulfil their intended function beyond the wavelength of $\lambda = 1550$ nm for which they were designed.
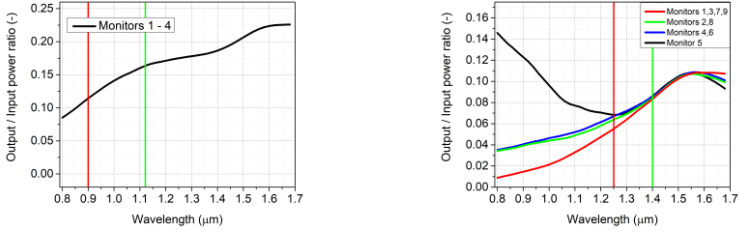
Fig. 1.3: Spectral characteristics as simulated by BPM, red lines signify a loss of -3 dB versus the maximum output value, and the green line indicates the point where the output maxima retain a correct distribution and sufficient separation: 1×4 splitter (left); 1×9 splitter (right).

1.3. Fabrication and Characterisation

For the 1×4 MMI splitter fabrication, IP-Dip photoresist was used in a single-step process based on DLW using TPA. The commercial Nanoscribe Photonic Professional GT laser lithography system based on DLW was the crucial technology for the fabrication of the MMI splitter. The IP-Dip photoresist was used in immersion laser lithography (DILL) mode, where the lens was immersed in a liquid photoresist. Fig. 1.4 shows an SEM image of the prepared 1×4 MMI splitter.
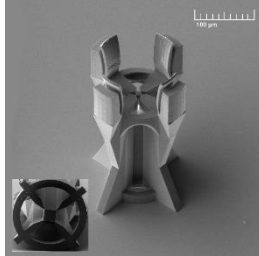

Fig. 1.4: SEM image of the fabricated 1×4 MMI splitter with square-profile tapered input waveguide and supporting structure. The inset image shows the detail of the output side of the splitter.

Characterisation of the modal distribution across the output part was done using a highly resolved near-field scanning optical microscope (NSOM). The near-field distribution near the output was measured in transmission mode. The measured distributions in Fig. 1.5 closely resembled the distributions acquired by simulations. More details about the fabrication and NSOM measurements of the 1×4 MMI splitter are available in our previous work [18].
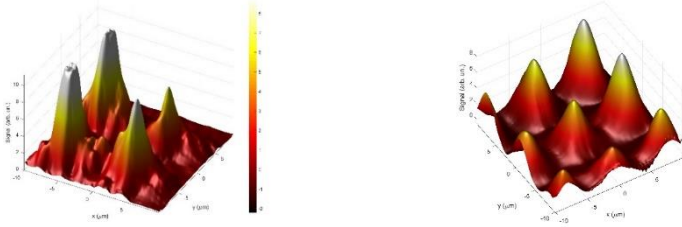
Fig. 1.5: 3D interpretation of a near-field distribution of the 1×4 MMI (left)
and of the 1×9 MMI (right).

The size of 1×9 MMI is outside the range of the maximum area measurable by NSOM, so one of the maxima is not present in the measured intensity distribution. Even in the cropped image, one can see that the 1×9 MMI splitter fulfils its function; the number of peaks and their separation are visible. The measured shape and intensity distribution reflect the simulated results.

1.4. Nonuniform Outcoupling Investigation

Both fabricated splitters show a bias towards one of the structure's corners, which was not present in the simulated characteristics. Three different possible causes for this phenomenon were identified: the off-centre position of the input fibre in relation to the input waveguide, the shift of the input modal field in the input fibre itself due to the bending of the fibre in the measurement setup, and the axial misalignment of input fibre in relation to the splitter structure. All of these probable causes were investigated using BPM simulations.

The position of the input waveguide in conventional MMI splitters is fixed in the centre of the multi-mode waveguide. Attaching the designed 3D splitters to the end of the optical fibre poses new challenges in the alignment of the input and the fibre. For simulations, the input fibre was diagonally off-centred from the central axis of the multi-mode waveguide (Fig. 1.6).
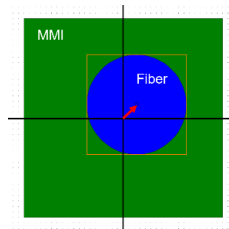

Fig. 1.6: Schematic of the off-centre input fibre with the direction shown by the red arrow.

The influence of the fibre offset on the optical power of the MMI without input taper can be seen in Fig. 1.7. In a 1×4 splitter, the lowest output crosses the half-power mark (-3 dB

compared to the same output without offset) at an offset value of 1.7 µm. In the case of a 1×9 splitter, this occurs at 2.4 µm.
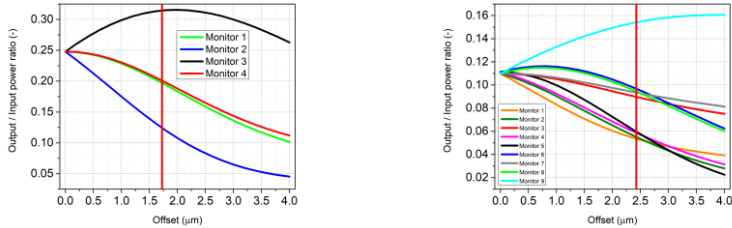

Fig. 1.7: Power distribution at the end of the MMI couplers against varying offsets of the input fibre: 1×4 MMI (left); 1×9 MMI (right).

Modal field distributions of both splitters with the maximum allowed fibre offset are shown in Fig. 1.8. The output modal field positions are shifted, and their shapes show some degree of distortion.
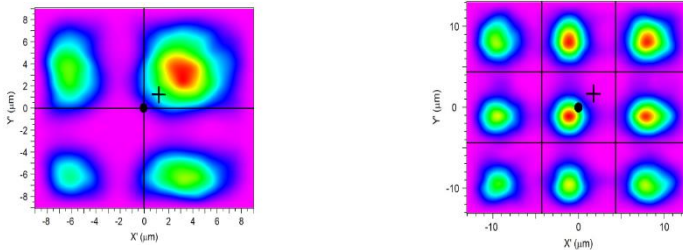

Fig. 1.8: Output modal field distributions at the end of the splitters with off-centred fibre. The black dot denotes the central axis of the MMI, and the black cross denotes the central axis of the input fibre: 1×4 splitter with an offset of 1.7 µm (left); 1×9 splitter with an offset of 2.4 µm (right).

The NSOM measurements of prepared structures show uneven splitting to the extent that should not be possible with alignment achieved by using a support structure with a fibre socket. Furthermore, the input tapers were prepared in a single fabrication step, reducing any possibility of misalignment. Therefore, the offset input fibre is not the leading cause of the observed distortion.

Another probable cause is the bending of the input mode. The bending can result in distortion of the modal field, which could lead to altered splitter function. Since the DLW-prepared input taper is generally straight and relatively short for any bending to occur, the origin could only be the fibre bend. BPM simulation results (Fig. 1.9) show modal distortion at bend radii around 4 mm. At bend radii > 8 mm, the distortion of the modal field does not occur to a degree that would lead to the measured shift in output maxima of prepared MMI couplers. The maximum shift is negligible even at radii lower than 4 mm. Thus, it can be concluded that the bending of the input fibre does not contribute significantly to the observed distortion of the output maxima.
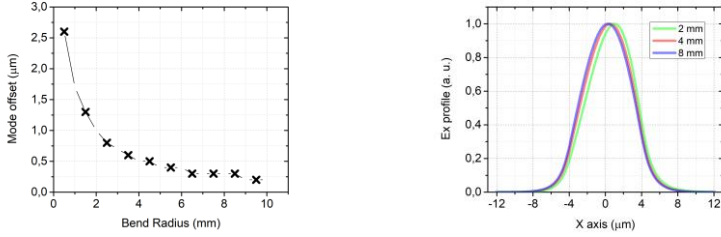
Fig. 1.9: Maximum offset of the mode in relation to the simulated bend radius (left); Simulated E_x mode profiles of SMF-28 fibre with bend radii of 2 mm, 4 mm, 8 mm (right).

The last probable cause investigated was the axial misalignment of the fibre to the prepared structure. The attached structures show a deviation from the central axis of the SMF (Fig. 1.10). This deviation could be caused by the imperfect attachment of the fibre or by the deformation of the prepared structure compared to the design.
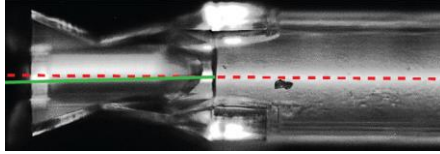
Fig. 1.10: Attached MMI splitter with supporting structures; the red line shows the central axis of the input fibre, and the green line shows the central axis of the MMI splitter [19].

The ageing of the polymer could also cause shrinkage and, thus, undesired deformation of the structure. Regardless of the cause, the effect of light propagating through a structure that is not perfectly straight could result in non-uniform outcoupling. The simulations of this case were done by offsetting the end of the MMI coupler from its start along the X and Y axes (Fig. 1.11). Increasing offset results in increasing nonuniformity of output fields.
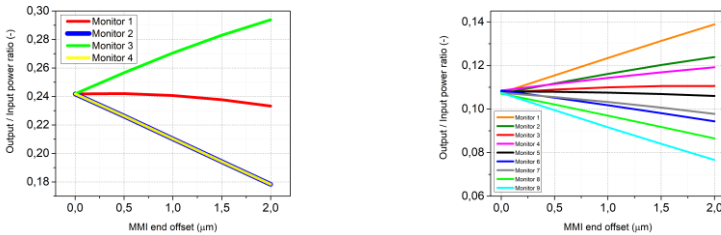
Fig. 1.11: Power distribution at the end of the MMI couplers against varying offsets of the input fibre: 1×4 MMI (left); 1×9 MMI (right).

The output mode field distributions at an offset of 2 µm show similar nonuniformity observed in NSOM measurements (Fig. 1.12). The shape of the output field is retained with

minimal distortion, while the maxima values decrease towards one of the corners of the MMI coupler in both 1×4 and 1×9 splitters.
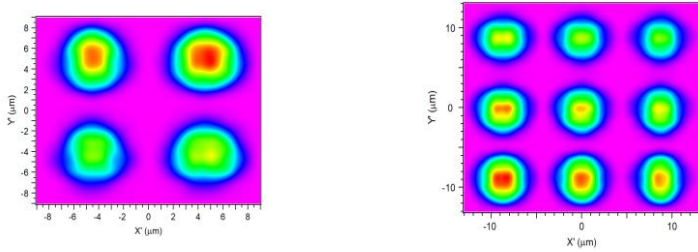
Fig. 1.12: Output modal field distributions at the end of the MMI couplers
at an offset of 2 µm: 1×4 MMI (left); 1×9 MMI (right).

Based on the presented simulation results, the most probable cause of output nonuniformity is the deviation of the DLW printed structure axis from the fibre axis. The most likely cause is the imperfect attachment of the fibre. This could be remedied by adding a longer input taper or a sufficiently long straight waveguide section of IP-Dip after the fibre termination point. Both proposed solutions require additional fabrication steps due to the height limitation of the available technology.

2 Optimisation of a Fabry-Pérot Interferometer-based Sensor

Demand for miniaturisation of sensors and requirements for electromagnetic interference (EM) immunity make a case for an optical sensing element such as the Fabry-Pérot interferometer (FPI). These devices have been used to detect a number of physical quantities such as temperature, magnetic field, and pressure [20]. FPIs have also served as mechanical displacement and gas presence sensors [21]. Integrating an FPI with an optical fibre by placing it on a fibre tip to form a lab-on-fibre sensor has been a topic of recent research [22, 23]. Novel fabrication methods and materials, such as polymer direct laser writing (DLW), have to be used to prepare these devices, but the versatility of this approach outweighs its increased complexity in the case of experimental structures.

The object of the investigation described in this chapter was a 3D Fabry-Pérot resonator structure prepared by DLW at the tip of a single-mode fibre. The original design set the air resonator to 38.75 µm and was fabricated using the Nanoscribe Photonic GT system. The structure was made of IP-dip polymer with a refractive index value of $n = 1.53$ (at $\lambda = 1550$ nm). The cladding and the resonator cavity consisted of air with $n = 1$. The prepared device can be divided into three sections along the Z-axis (Fig. 2.1).
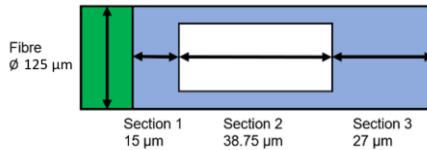
Fig. 2.1: Schematic of the DLW prepared device: IP-Dip (blue), input fibre (green).

The goals of the investigation were to use obtained measurement data of prepared FPIs to create a simulation model that would replicate the behaviour of actual structures and then utilise it in optimising the geometry of the original design and in the testing of different data interpretation methods.

The University of Žilina provided the IP-Dip structures used in the measurements. The measurements of temperature and pressure responses were provided by VSB - Technical University of Ostrava.

2.1. Working Principle of a 3D FPI Sensor

To create a better picture of potential optimisation avenues, one needs to understand the basic working principle and the figure of merits of the device in question. In its simplest form, the investigated FPI consists of two parallel mirrors within which light undergoes multiple reflections. The

At each 2π phase change between mirrors, resonance occurs, which results in an interference maximum in the spectrum. The separation between two adjacent maxima can be expressed in terms of wavelength as [24]:

$$\Delta\lambda = \frac{\lambda_0^2}{2nL\cos\theta + \lambda_0} \approx \frac{\lambda_0^2}{2nL\cos\theta}. \tag{2.1}$$

$\Delta\lambda$ is the free spectral range (FSR) of the FPI (Fig. 2.2), which determines the usable range of the structure, as overlapping the maxima introduces ambiguity in the measurement. The thing to note from the equation is that the FSR is inversely proportional to the optical cavity length nL.
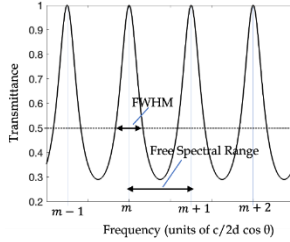
Fig. 2.2: Transmittance spectrum of an FPI with FSR and FWHM and resonant peak position highlighted [25].

The resolution of the interferometer is given by the FWHM of the interference maxima, which is dependent on the reflectivity of the mirrors. This parameter is called the finesse of the resonator F.

$$F \equiv \frac{\pi\sqrt{R}}{1 - R}. \tag{2.2}$$

The FWHM of resonance peaks is proportional to the finesse and is expressed as:

The sensing capabilities of the FPI take form in the spectrum shift with respect to the environmental conditions. The relation between the spectral shift of the structure and the change in environment temperature is given by:

$$\frac{d\lambda_m}{dT} = \frac{4}{2m + 1}\left(\frac{dn}{dT}L + \frac{dL}{dT}n\right), \tag{2.3}$$

where dn/dT is the thermo-optic coefficient of the cavity medium and dL/dT is the thermal expansion coefficient of the material [26].

Several devices, such as the investigated FPI, have been prepared to this day. The most relevant examples of these devices are the single solid polymer resonator and dual air-polymer resonator structures realised by Smith et al. [27]. The configuration of the dual

14

resonator devices is most similar to that in the investigated structures, where a thick IP-Dip layer forms the second mirror and an additional solid IP-Dip resonator. Smith et al. state that the dual resonator device provides an open cavity for analyte measurements while simultaneously using the second solid IP-Dip cavity spectrum as a reference. They stated that calculating the effects in the polymer cavity and subtracting them from the whole structure would provide a clearer picture of the effects in the open cavity. A detailed description of the methods used to analyse separate resonators is not provided.

2.2. Initial Measurements

The IP-Dip FPI samples provided by the University of Žilina were characterised by microscopy and spectral measurements under room conditions. The goal of the microscopy was mainly to verify the length of the air cavity of the resonator and to show any deviations from the provided design. The spectral measurements then served as the basis for the simulation and verification of the simulated characteristics.

Microscopy measurements were performed with an optical microscope (Keyence VHX7000) and SEM (Zeiss LEO 1550). The cylindrical shape of the structures proved to be challenging to capture correctly. The shallow depth of field in the optical microscope and the partial translucency of IP-Dip made it impossible to capture the whole structure in focus within one exposure. The positioning of the sample also posed a challenge compared to planar structures due to the rotation of the sample in relation to the viewpoint.

The optical microscope images show the 3-layer structure of the FPI (Fig. 2.3). IP-Dip is clearly distinguished from the SMF by the yellow colour. The distance measurements of the sections and the fibre agree with the expected dimensions.
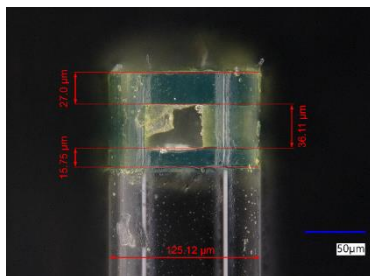
Fig. 2.3: FPI (Sample 14) with the cavity opening visible and dimension measurements.

The sample had to be covered with a thin gold layer for the SEM imaging to ensure proper discharge, as the polymer conductivity was low. Thus, the SEM imaging was destructive to the sample. This could be avoided by using a better vacuum or a different SEM, none of which was available at the time. SEM images (Fig. 2.4) show the same general structure of the FPI. The better resolution of the SEM provides a clear image of the striations caused by DLW technology. The average dimensions of each section obtained by measurement were

14.93 µm (Section 1), 38.17 µm (Section 2), 26.59 µm (Section 3), and 79.88 µm (Total length).
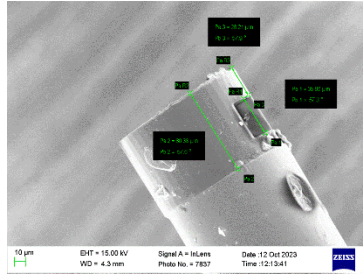
Fig. 2.4: SEM images of FPI (Sample 15) with dimension measurements.

After microscopy, the available samples were measured in terms of insertion losses in the spectral window of 1460-1580 nm (Fig. 2.5). The results agreed with the expected spectral characteristics obtained from the literature. In all cases, the double peaks of the two resonators were present.
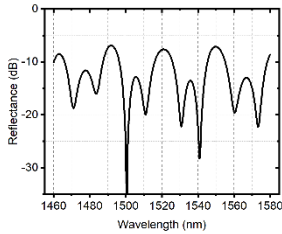
Fig. 2.5: Measured reflectance of selected DLW-prepared samples.

Initial measurements and microscopy images formed a valuable basis for subsequent model formulation and confirmed that the overall structure and material characteristics are mostly retained in all samples.

2.3. Simulation Models

Three different methods were used to verify the reflectance of the prepared device: Transfer Matrix Method (TMM), Rigorous Coupled-Wave Analysis (RCWA), and Finite-difference Time-domain method (FDTD). The first aim was to set up a model to replicate the reflectance measurements as accurately as possible and identify deviations of the simulated characteristics from the measurements.

The semi-analytical method RCWA utilises the 2D model, the boundaries of which are periodic on the X-axis. This method still does not consider the sidewalls of the structure, but its nature enables the shaping of the material interfaces while being less

computationally demanding than FDTD. The schematics of the different models are depicted in Fig. 2.6.
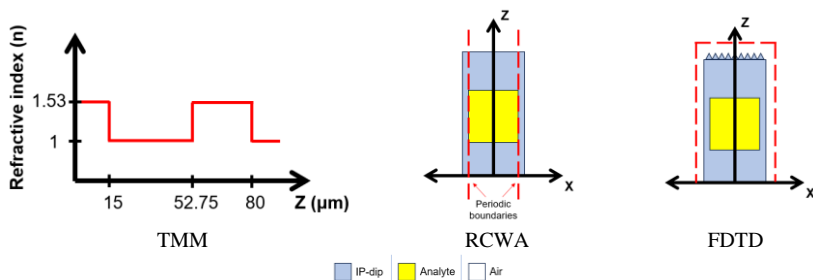
Fig. 2.6: Schematics of the simulation models: a 1D model for TMM; Periodic boundary model for RCWA (left); Model with included sidewalls and scattering structure for FDTD (right).

The model dimensions were defined according to values in Fig. 2.1. The refractive index of IP-Dip was set to 1.53, as its value does not change significantly in the simulated spectral region (1480 – 1640 nm). The resulting reflectance characteristics are similar to the measured ones for each method (Fig. 2.7).
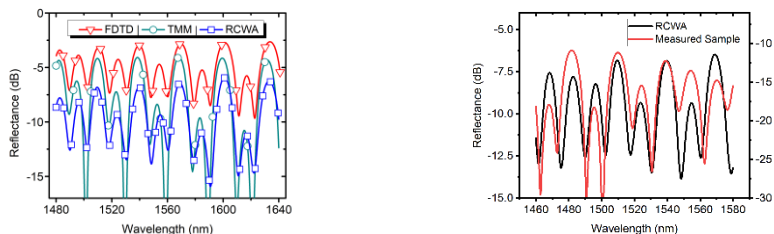
Fig. 2.7: Comparison of the simulation methods used (left); Comparison between measured reflectance and RCWA simulation (right).

The main object of focus, the spectral peak position, is retained between the simulation and the measurements. This observation suggests that the reflections from the sidewalls of the structure do not contribute to the overall function of the device in a significant manner and that the measured structure resonator lengths did not deviate from the provided figures considerably (at most by degree of 10^{-2} µm).

17

2.4. Possible Optimisations of the FPI

Taking into account computational requirements and the accuracy of the simulation against the measured reflectance of the device, RCWA was chosen for further simulations of different air resonator lengths and analyte refractive index changes. RCWA simulations were realised for dual and single-resonator FPI designs. The single resonator design was achieved by setting the Section 3 length to 0.75 µm, thus reducing its influence on the spectral response of the whole FPI. Further simulations show a linear peak position change in the case of resonator deformation in both single- and dual-resonator designs (Fig. 2.8). The values representing the phase shift of *2π* for both simulated structures are ~0.8 Δµm in the case of the resonator length deformation. A notable change in the peak position shift can be observed between the two designs. The single resonator structure shows values of peak shift that are twice higher than the original design.
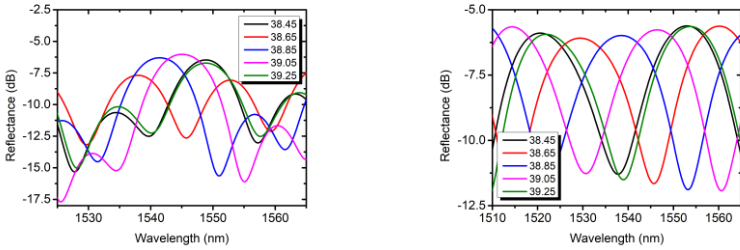
Fig. 2.8: Simulated spectral characteristics of resonator length change for the original design (left) and the 0.75 µm resonator design (right).

The overall sensitivity values for both simulated parameter changes reflect the reduced peak shift between the single-resonator and original designs (Fig. 2.9). The decreased sensitivity and distortion of the spectral peak positions are caused by the influence of the second resonator in the original design.

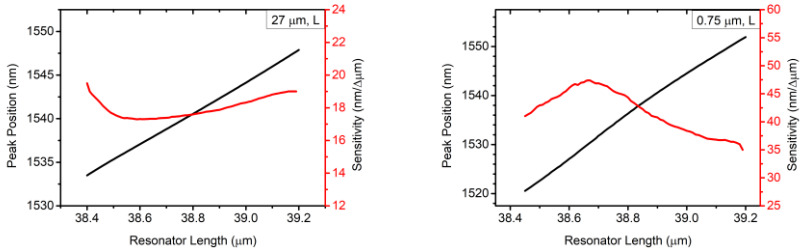Fig. 2.9: Peak position and sensitivity characteristics in response to changes in resonator length for the original design (left); and the 0.75 µm resonator design (right).

The first subject of optimisation was the second resonator itself. The additional resonance occurs between the polymer-air interfaces of the 3rd section of the prepared structure. The refractive index of IP-Dip cannot be adjusted using the available fabrication method (DiLL). Due to this, the reflectivity of mirrors is considered constant at a value of 4.39 % (obtained by Fresnel equations).

The DiLL process facilitated by Nanoscribe Professional GT has limits in the resolution and range of the print. The resolution limit is given by the laser focus spot size, 0.2 µm in the XY plane and 0.6 µm in the Z axis. The range limitation concerns the Z-axis, where a maximum of 300 µm is achievable in a single step. The mechanical integrity of the layer also limits the minimum thickness of the realisable layer. With technology limitations in mind, different thicknesses of the layers were investigated.

Setting the central wavelength as $\lambda_0 = 1560$ nm, which represents the middle of the measured spectrum, the FSR values of $\Delta\lambda = 30.781$ nm in the case of the air resonator and $\Delta\lambda = 28.910$ nm in the case of the IP-dip resonator are obtained (Fig. 2.10, left). In the original design, the resonators are joined together, and measuring them separately is impossible. Dividing the simulation domain into two parts, the reflectance of each resonator can be analysed in terms of FSR. The resulting spectra for each separate resonator are depicted in Fig. 2.10, left. By multiplying the separate resonator characteristics, one obtains a characteristic with peak positions and shapes remarkably similar to the original structure (Fig. 2.10, right). This confirms the intermodulation between the two resonators.
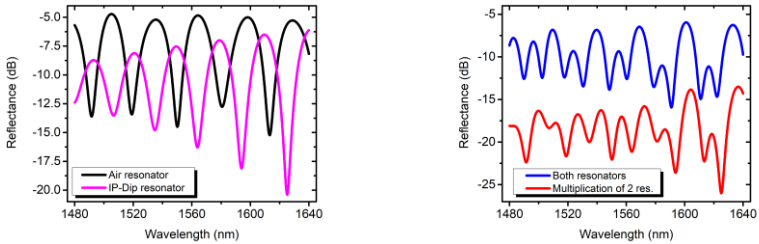
Fig. 2.10: Reflectance spectra of each resonator (left); whole structure and multiplication of two separate resonators (right).

The intermodulation of the resonators cannot be avoided, but its effects depend on the second resonator's length and, thus, its FSR. The ratio of FSR of individual resonators in the original design results in a halving of the FSR of the whole structure, which halves its sensitivity.

If the FSR of the second resonator is increased to values much greater (by decreasing its length) than the measured spectral range, it is possible to fit the reflectance pattern of the air resonator across the broad maximum of the thin IP-Dip resonator. However, the thickness of such a resonator (significantly below the used wavelength) is not readily achievable using the available technology. A compromise thickness of 5.4 µm,

which is mechanically sounder, provides a spectral window between 1550 - 1610 nm (Fig. 2.11, left). Another way to reduce the second resonator influence would be to decrease its FSR (by increasing its length) to a degree where a large number of peaks fit under one peak of the air resonator (Fig. 2.11, right). Separating the two resonators, FSR makes it possible to filter out the long resonator's higher frequency signal and obtain the air resonator's peak positions.
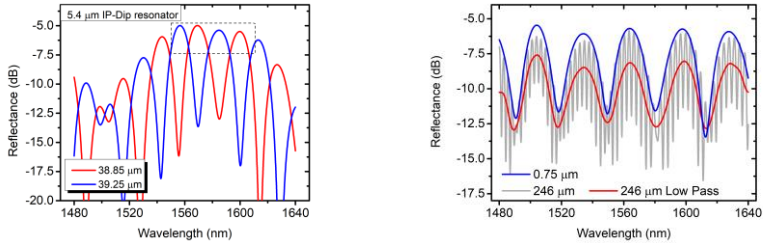
Fig. 2.11: Spectral responses with two optimised IP-dip resonator lengths

Another option to reduce the influence of the IP-dip resonator would be to minimise reflection from the last interface. This can be achieved by scattering the propagating light using small structures that optically break up the interface between the polymer and the air. A similar approach was used in the FPI structure prepared by Goraus et al. [28].

The simulation model used was realised using 2D FDTD. The model consisted of the FPI and an array of triangular/trapezoidal objects forming the scattering structure. The parameters FDTD tested were the objects' base width and the angle of the sidewalls (Fig. 2.12). The tip width was fixed to 0.2 µm, the minimum size achievable by the DiLL process.
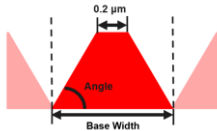
Fig. 2.12: A single period of the scattering structure (right).

The results of the 5.4 µm resonator with scattering structure (Fig. 2.13) agree with the experimental results of Goraus et al. [28]. The presence of the second resonator causes the deformed peak in the measured spectra. A similar peak is present in the 5.4 μ m IP-dip resonator simulation, but its position is shifted towards higher wavelengths. This suggests a slight mismatch in the length of the actual resonator compared to the simulation. The added length of the scattering structure probably causes the mismatch. Considering all the parameters and effects described in this chapter, the prepared FDTD model reflects the FPI as a whole accurately and verifies the function of the scattering structure as a means to eliminate the reflection from the last interface.
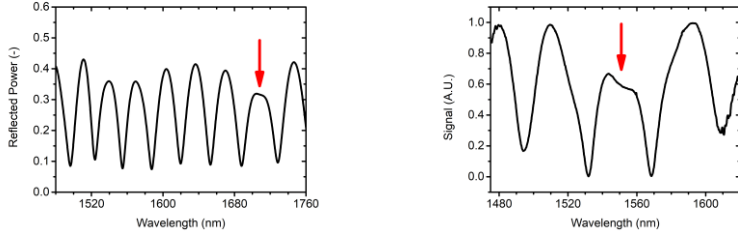
Fig. 2.13: Broader spectral response of the 5.4 µm IP-Dip resonator with a deformed peak at ~1710 nm (left); Spectral response of a similar IP-Dip FPI prepared and measured by Goraus et al. [28] with the deformed peak at ~1550 nm (right).

The reflectivity value of the IP–Dip–air interface (4.39 %) makes for a low-finesse FP resonator. Such resonators' power transfer characteristics (transmittance, reflectance) approach the shape of a sine wave with the resonator's FSR being equal to the approximated sine wave period in a sufficiently narrow spectral range. If the FFT is used on the measured spectral window, the approximated sine wave manifests as a peak in the resulting frequency spectrum.

For demonstration, Fig. 2.14 depicts the spatial frequency spectrum of the FPI original design and the 246 µm IP-dip resonator design obtained from the RCWA simulation results. Both spectra show two pronounced peaks that correspond to each of the two resonators. Both air resonator peaks are at a frequency of 0.03136 nm^{-1}, which translates to a period of $T = 31.88$ nm, which is close to the FSR value $\Delta\lambda = 30.875$ nm obtained from the reflectance spectrum. What manifests as the second peak in the case of a 27 µm resonator is most likely the higher amplitude of the second harmonic frequency of the whole structure.
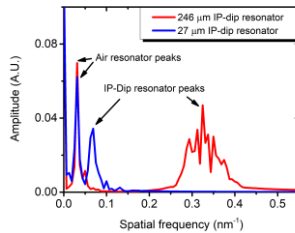
Fig. 2.14: FFT spectra of two dual resonator FPI structures

Since the resolution of a spatial frequency spectrum is given by the range of the signal in the radiation spectrum, the peaks in Fig. 2.14 do not precisely reflect the FSR values of the resonators. However, tracking the phase shift at the spatial frequency of the air resonator is possible. The phase value changes both with the air cavity RI value change and with the resonator length change (Fig. 2.15). In the case of the 0.75 µm resonator, the change is linear. Linearity is retained in the optimised 5.4 µm IP-dip resonator design. In the original

21

design, the change is linear up to 65º; then the FPI shows a steeper drop up to 270º. This is most likely caused by the similar FSR values of the individual resonators in conjunction with a short reflectance measurement, resulting in wide FFT bins. The phase change of 360º corresponds to the peak shift over one FSR in each simulated FPI.
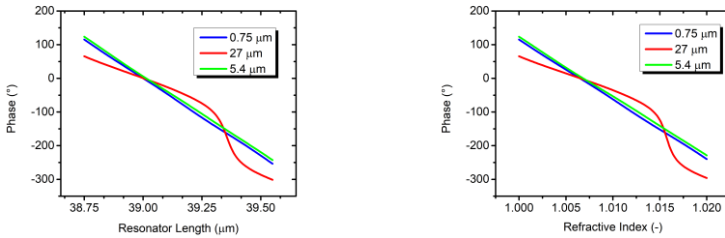
Fig. 2.15: Phase change against varying air cavity length values (left) and varying air cavity refractive index values (right).

Assuming that the refractive index of air does not change during the initial measurement, the simulation models were used to approximate the values of air cavity length. The dimensions of the other sections were defined as designed. The resulting values are primarily within 0.3 µm compared to the measured values. In the case of sample no. 9, the difference is 0.5 µm. This points to the significance of the air cavity resonator in the overall spectrum shape.

Since the material used also exhibits a thermo-optic effect of -2.6×10–4/K (at 1550 nm), the change in its refractive index influences its spectrum. The phase change according to the changing material refractive index was also simulated. The tested values were chosen assuming an IP-Dip refractive index value of 1.53 at room temperature.

After the simulation and analysis of spectra using the dimensions of each sample in Table 3.1, the refractive index values for each sample were obtained with respect to the phase. Each sample (except for No. 14) showed phase values corresponding to ~1.528, equivalent to an ambient temperature of 27.7°C (assuming RI of 1.53 at 20 °C).

Overall, this approach enables spectral separation of the measured data and thus enables evaluation of each used resonator separately, provided that the measured spectrum is broad enough to resolve their respective peaks.

2.5. FPI Environment Change Response

The simulations described so far were based on FPI measurements at room conditions described at the beginning of this chapter. These FPI structures were prepared with the aim of sensory applications. Thus, spectral characterisation according to environmental changes was realised by the team at VSB Ostrava. The tested environmental conditions in this work are the temperature change, ranging from 5 °C to 50 °C with a step of 5 °C, and the air pressure change, ranging from ~0 bar to 5 bar with a step of 0.5 bar.

The measured spectra were analysed in terms of peak position and spatial frequency. The phase and peak position values were then compared against the phase values obtained from the RCWA simulation to obtain the air resonator lengths of the measured structures. The temperature change spectra (Fig. 2.16, left) are consistent with the initial measurements presented at the beginning of this chapter (Fig. 2.5). Some degree of noise is present in all measurements, mainly in the upper part of the characteristics. All of the samples show a red shift with increasing environment temperature. All samples also show movement at peak levels, consistent with previously observed intermodulation between the two resonators. The peak position shift and spatial frequency phase values were obtained from a series of measurements for each sample (Fig. 2.16, right). The phase values obtained generally follow the peak position values. The similarity of characteristic shape shows that the sine wave approximation of the air resonator closely resembles its measured spectral shape.
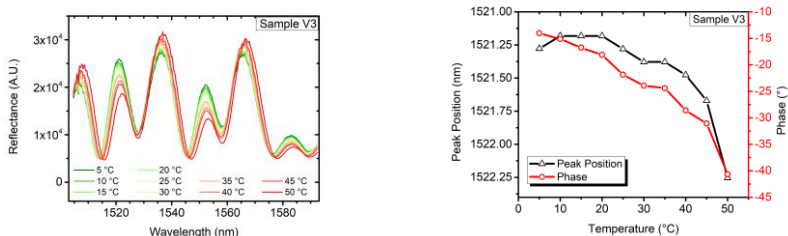
Fig. 2.16: Temperature change spectral measurements of FPI sample V3 (left); Peak position and phase shift against temperature (right).

Spatial frequency analysis provides information about the resonator length more readily than the peak position. When the phase values of each sample are compared, it is apparent that each sample differs slightly (Fig. 2.17, left). In all the samples, the phase value decreases with an increase in temperature. The thermo-optic effect present in IP-Dip suggests an opposite trend: the phase value should also increase with increasing temperature. Since this is not observable in the measurements provided, the results point to thermal expansion being the main contributor in this design of an FPI.
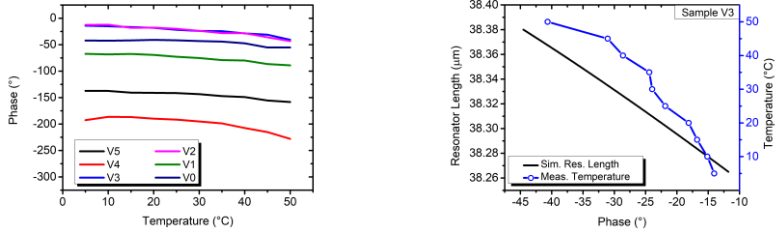
Fig. 2.17: Phase values of each sample against temperature (left); Simulated resonator length and measured temperature values of FPI sample V3 against obtained phase values (right).

The simulation of different resonator lengths and a detailed view of the phase values obtained from measurements are presented in Fig. 2.17 (right). The decrease in phase values with increasing temperature is present in all samples. The decreasing trend is most likely due to the shrinking air cavity length with increased temperature. The measured characteristics show a degree of nonlinearity, which is not present in the simulated results, with the nonlinearity of samples. These nonlinearities could be attributed to the thermo-optic effect of IP-Dip.

The pressure change spectra in Fig. 2.18 (left) show that the pressure change does not introduce unexpected peak position shifts in a single sample. A detailed view of the peak position shift and phase shift shows the linear characteristics of sample V3 (Fig. 2.18, right). The pressure change characteristics show a higher degree of linearity than temperature measurements.
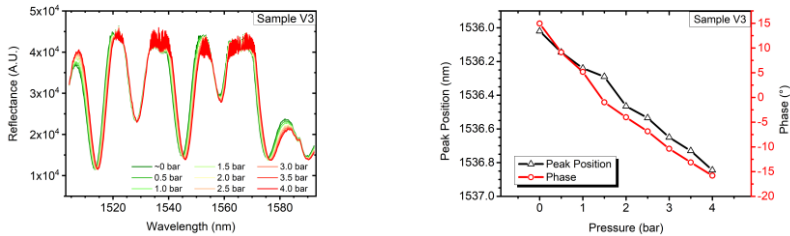
Fig. 2.18: Pressure change spectral measurements of FPI sample V3 (left); Peak position and phase shift against temperature (right).

The simulation of different resonator lengths and a detailed view of the phase values obtained from measurements along with simulation of different resonator lengths are presented in Fig. 2.19. The decrease in phase values points to air resonator elongation. The pressure change curve follows the simulation of the resonator length more closely than in the case of a temperature change. This indicates a closer relationship between the pressure and the optical air resonator length.
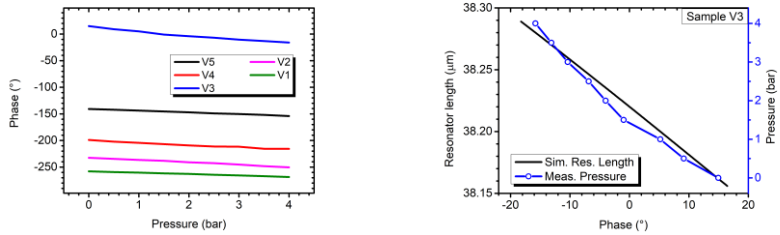
Fig. 2.19: Phase values of each sample against pressure (left); Simulated resonator length and measured temperature values of FPI sample V3 against obtained phase values (right).

3 Photonic Devices Utilising Plasmonic Effects

This chapter presents two material platforms (IP-Dip and silicon oxynitride) and evaluates their viability in supporting a plasmon-enabling metal layer regarding refractive index compatibility and surface roughness requirements. The surface roughness was represented by AFM-acquired roughness profiles of respective materials in various stages of fabrication processes.

3.1. Polymer-based Photonic-plasmonic Device

The angular dependence of the SPP limits the design of a photonic device. The design process mainly focuses on achieving the incident angle needed to excite the plasmon within the constraints of available technology, provided the material platform supports SPP formation and propagation at the material interface layer. Polymers that enable novel fabrication methods, such as DLW, alleviate some of these constraints while exacerbating others. The following chapter focuses on plasmonic photonic sensing structures based on IP-Dip. Its viability in terms of refractive index matching and surface roughness is evaluated using simulation methods.

   The IP-Dip structure serves as a base for the SPR-based fibre probe. The device was optimised for use with a wavelength of $\lambda = 785$ nm. Simulations were carried out using the FullWAVE simulation tool in the RsoftCAD suite. The simulation models used were inspired by the work of P.S. Menon et al. [29]. The simulations aimed to investigate the behaviour of IP-Dip in relation to the thickness of the gold layer, to find the optimal angle value for SPR to occur, and to simulate the response of the optimised structures to changes in the values of the analyte's refractive index.

   Due to how FullWAVE handles the light source's rotation, two simulation models were created. One has a rotating interface between the two dielectrics (used in angular interrogation), and the other has a fixed interface, a rotating light source, and a rotating monitor (used in wavelength interrogation).
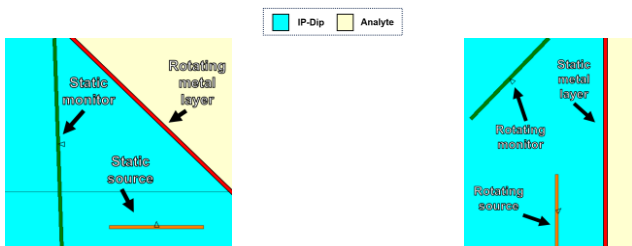
Fig. 3.1: Models used for FDTD simulations: model with a rotating interface on the left, model with a rotating source and monitor on the right.

The grid size was set to 10 nm in the entire simulation domain to achieve at least four grid points at the gold interface layer. This approach should provide greater accuracy. Since the Yee cell grid required for FDTD simulation does not support non-uniform element sizes, the whole simulation domain is defined with a relatively small 10 nm step. This increases the computational demands of the simulations.

In the first step, a range of gold thin film thicknesses was simulated, obtaining angular interrogation characteristics. The dielectric medium used in the simulations was air with a refractive index value of $n = 1$. The material used as a prism is IP-Dip with $n = 1.53$. The thin film thickness was varied from 30 nm up to 90 nm. The angle sweep range was set from 35° to 50°. The angular interrogation results show dips in normalised power values with minima at around 43.2°, as shown in Fig. 3.2 (left). The thickness of the layer affects the overall transmitted power outside the SPR region and the minimum power transmitted in the SPR region due to the reduced reflection of the thinner gold layers. Higher values of thickness result in a higher amount of light reflected, less pronounced dips in the transmitted power, and a smaller range of angles where the decrease of power takes place. Next, using the optimal values determined by angular interrogation, spectral characteristics were simulated for a range of analyte refractive indices (1.0 – 1.005) (Fig. 3.2, right). The change in the minimum position in the spectra was observed according to the change in the analyte refractive index. The gold layer thickness was set to 40 nm because this value showed the lowest power throughput in the SPR region.
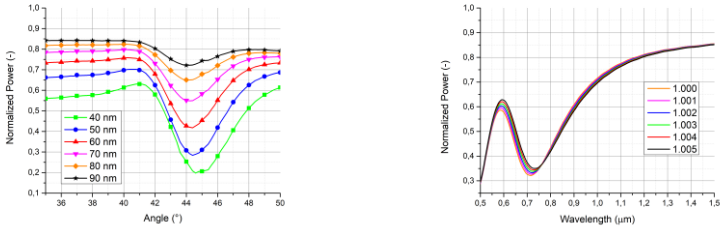
Fig. 3.2: SPR response curves for various thicknesses of the gold layer against changing the incident angle (left); Spectral characteristics of a range of analytes (right).

The results thus far show minima positions shifting toward longer wavelengths with increasing refractive index values. The overall power coupled into the surface plasmon decreases with an increasing refractive index value. Simulations show an average wavelength sensitivity of ~3500 nm/RIU. Overall, FDTD simulations show that SPP excitation is possible with air-based analytes.

The DLW fabrication process results in striations in the surface caused by scanning the laser during the 2PP of the voxels. The simulations aimed to evaluate the effect of the resulting roughness on the excitation and propagation of SPP. A FEM-based approach was used in the subsequent simulations due to the limitations of FullWAVE FDTD implementation, namely the angled plane wave excitation handling, non-rectilinear gridding absence, and high computational demands. The FEM-based simulations used

COMSOL Multiphysics, which supports advanced gridding (Fig. 3.3, left) and simple geometry import. This enables a better representation of a rough surface in the simulation by using more elements in the region of interest, cutting computation demands down. The surface roughness model used was based on the work of Frei W. [30], depicted in (Fig. 3.3, right). The values monitored using the model are Reflectance (R), Transmittance (T), Absorptance (A), and their total.
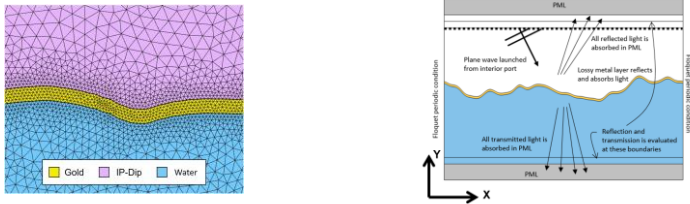
Fig. 3.3: Nonuniform FEM grid generated by COMSOL Multiphysics (left); The computational domain of the model used for the simulation of the surface roughness effect (right).

The parametric curves representing the striated surface of the developed IP-Dip layer come from an article by Smith et al. [31]. The article provides three cross-sections obtained from AFM measurements (Fig. 3.4). The authors state that the roughness of the surface is approximately 60 nm with a peak-to-valley difference averaging 120 nm.
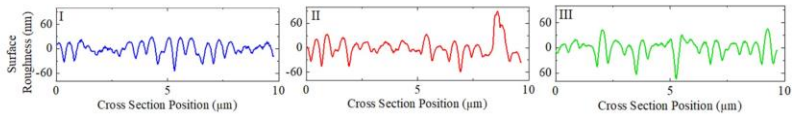
Fig. 3.4: Three cross sections across the surface of the IP-Dip film measured by AFM [27].

First, the ideal case of a surface with zero roughness was simulated using fixed refractive values for both water (1.33) and IP-Dip (1.53). The gold was modelled from data by Johnson and Cristy [32]. The model's angular characteristics show the SPR dip at 70.1°. This angle value was then used for spectral simulations (Fig. 3.5, left|). The transmittance of the interface is zero in the region of interest. The coupling to the SPP represented by the absorbance characteristic is around 90%. Afterward, the AFM cross-section was introduced, and the spectral characteristics were simulated again (Fig. 3.5, right). The SPR dip is broadened and less pronounced than the ideal, increasing from ~10% of the power reflected to ~25%. The rest of the monitored values (R, A) show a more significant deviation from the ideal. The absorbance value reduction is mainly due to the lower confinement of the SPP, which is either not coupled to the interface at all or lost during propagation.
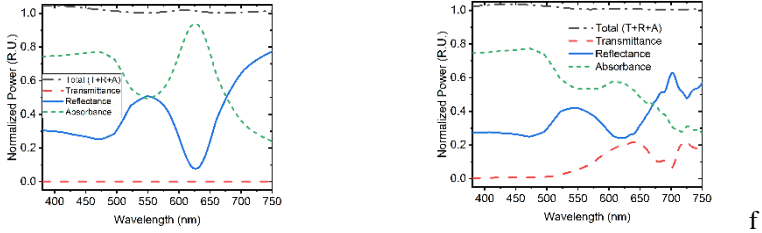
Fig. 3.5: Spectral characteristics of the ideally smooth interface (left); Spectral Characteristics of cross-section No. 2 (right).

The ideal interface simulation results showed that IP-Dip should be a viable candidate for SPP sensing for air and water-based analytes in the visible part of the optical spectrum. However, the used simulation models may skew the obtained results to be closer to the ideal characteristics as the approximations in dimensionality, and the metal layer uniformity are not representative of the actual structure. Further research in angled IP-Dip surfaces and thin layer deposition is needed to assess the viability of this approach accurately. As the means needed to realise this kind of research were not available to the author at the time of writing this thesis, the question of viability is beyond the scope of this study.

3.2. SiON-based Photonic-plasmonic Device

At this date, the Institute of Electronics and Photonics at the Faculty of Electrical Engineering and Information Technology of the Slovak University of Technology in Bratislava (ÚEF FEI STU) has sufficient facilities to carry out research in the silicon oxynitride (SiON) material platform. A detailed study of the surface and material characteristics of SiON was performed using the knowledge and capabilities present. The goal of this study was to experimentally prove the capabilities of the prepared SiON films to support the formation and propagation of SPP. The further goal is modelling the structure based on fabrication parameters and the design of plasmonic-photonic sensing devices such as a previously proposed SPR-based multi-mode waveguide sensor [33]. The following chapters present an overview of the available SiON fabrication process and surface roughness simulation models based on tested experimentally prepared thin films. This section discusses the technological processes employed in the fabrication of optical waveguides, focusing on the processes used in ongoing SiON research at ÚEF FEI STU.

Generally, the fabrication process can be divided into three stages: thin-film deposition, photolithography, and etching. These are the steps that are present in most silicon waveguide fabrication processes. After the core layer is fabricated, the cladding layer is deposited on top if specified. The metallisation process is added because of the plasma etching technique, where metallic mask material plays a crucial role in the final

29

product. The complete fabrication process of the SiON waveguide realised at ÚEF FEI comprises these steps:

1. Deposition of SiO₂
2. Deposition of the SiON optical waveguide core layer
2. Metallisation
3. Photolithography
4. Wet etching of the metal layer
5. Plasma etching of the SiON l;ayer
6. Deposition of the SiOx cladding layer

The roughness of the SiON films was evaluated against three different process parameters. NH₃ flow rate during deposition, duration of deposition. All of the layers were deposited onto Si substrates. The layer roughness was measured using AFM, and the thickness was verified by SEM imaging. The surface profiles of the AFM were measured within two ranges (5x5 µm and 10x10 µm) and evaluated in a number of statistical quantities, namely average roughness (R_A), mean square roughness (R_{RMS}), maximum height (H_{MAX}). 5x5 µm measurements were used to acquire cross-sections representing the surface within the simulation domain.

First, four different flow rates of NH₃ (from 5 to 20 sccm) were tested. The deposition duration for this set of samples was 10 min. The thickness of the deposited layer for all samples in this set was measured to be ~750 nm. The different durations of deposition were then tested for two sets of samples with flow rates of NH₃ of 5 and 20 sccm. The durations tested ranged from 10 to 17.5 minutes with a step of 2.5 minutes. None of the samples varies significantly in roughness enough to suggest that the tested deposition parameters introduce significant changes in surface topology. The highest roughness values were measured in the sample with a deposition time of 17.5 min and an NH₃ flow rate of 5 sccm. The AFM images, out of which the statistical quantities were obtained, did not show any standout features between the samples. Similarly to IP-dip, three cross-sections were obtained from the measurement and used to simulate SPP excitation in the Kretschmann configuration. The refractive index of the SiON layers was assumed to be 1.55 in the visible range based on past ellipsometric measurements [34].

The simulation results show the presence of an SPR dip at 68.4° and 625 nm in the perfectly smooth interface. Introducing the AFM cross sections into the simulation shows a slight shift towards 69° in angle and 630 nm in wavelength (Fig. 3.6). The shapes of both characteristics remain mostly unchanged, with slight deformation and minor local power deviations, both in comparison to each cross-section and to the ideally smooth surface. The transmittance values are increased as expected based on previous simulations of IP-Dip roughness. However, the overall lower surface roughness of the tested profiles aids in keeping the absorbance and reflectance levels much closer to the levels of a smooth surface.
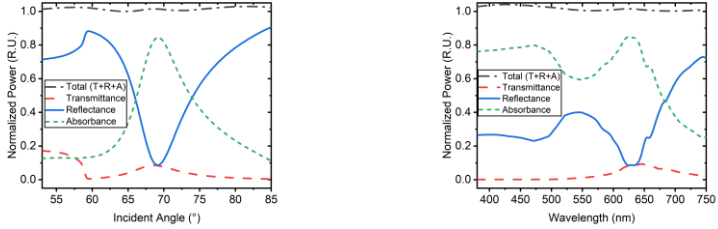
Fig. 3.6: Angular (left) and spectral characteristics (right) of the monitored values (cross-section No. 1).

The same surface roughness analysis and simulation approach were used to evaluate a set of SiON thin film samples that underwent ICP-RIE etching. The etching durations tested were 3, 6, and 12 minutes. The etched samples were not covered by a mask during the ICP-RIE process. The roughness values are increased after etching in all samples. The sample that underwent 12 min. etching yielded the highest measured values, where average roughness increased to 9.861 nm. Although the shorter etching durations increased the surface roughness, the statistical values varied only slightly from the samples before the etching. The simulation results showed that the SPR angle did not vary significantly from the ideally smooth surface and stayed around 68.8°. The reflectance values in the spectral simulations did not stray from the smooth measurements, and the SPR dip stayed at ~625 nm, similar to the smooth simulation. The influence of the roughness can be primarily observed in the absorbance and reflectance values in the region of interest. The 12 min. sample showed 25% transmittance values on average. This suggests a diminished coupling into the plasmon. The absorbance value confirms this. Higher transmittance values show a decreased efficiency of the rough surfaces, which diminishes further with the additional etching duration. Although the increased roughness does not affect the reflectance simulation values, the impaired coupling into the SPP would most likely result in reduced sensor performance. The reduced performance would most likely manifest itself as a reduced sensitivity to the refractive change of the analyte since a lower amount of light would be able to interact with the analyte.
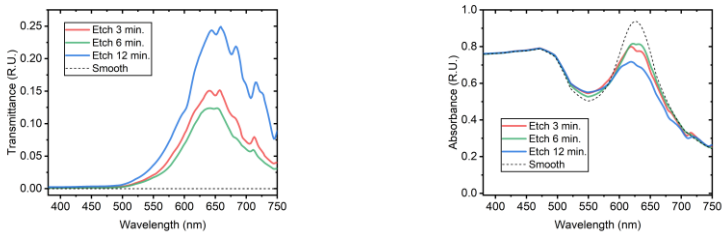
Fig. 3.7: Averaged spectral simulations of the rough surface with etch duration variation.

31

The possibility of tuning the refractive index of the SiON core layer and its optical properties in the visible part of the spectrum shows promise for its use in water-based analyte sensing. This is also apparent from the initial smooth-surface simulations of the material.

The PECVD deposition parameters investigated in this chapter included NH_3 flow rate and deposition duration. According to the simulation results, neither parameter influenced the SPP formation and propagation in a manner that would prohibit the intended function. The statistical quantities of average and RMS surface roughness remained at ~5 nm in each tested sample. This thin film structure without additional shaping can be used in ellipsometry using the Kretschmann configuration of the SPP coupling. The SiON layer with a gold layer thickness of 32 nm was tested in this manner at ÚEF FEI STU [34]. The ellipsometric incidence angle of 87° translates to 67.7° at the SiON-water interface. The wavelength used for ellipsometry was 645 nm. Simulating the experimentally tested configuration using the FEM model, the SPR resonance occurs at 66.6°. This slight difference between the measurement and simulation could be attributed to an unknown refractive index of the immersion oil or a deviation in the expected refractive index of the SiON layer. Nevertheless, the experiment confirms the formation of SPP on the SiON layer formed using the PECVD process used at ÚEF FEI STU.

The ICP-RIE etching simulation results showed higher transmission values for the sample with the highest etching duration tested (12 min.). This suggests that longer ICP-RIE etching results in a higher degree of surface roughness, which is detrimental to SPP formation and propagation.

Even if the simulation approximations (2D, ideal gold layer uniformity) are considered, the SiON thin films still show higher viability for SPP-based applications than the previously investigated IP-Dip platform. The lower surface roughness of the SiON films was achieved by different deposition and shaping methods, thanks to their material properties. Increased core layer roughness after the complete process of waveguide fabrication could affect the effectiveness of a supposed waveguide-based SPP sensor. Additional process investigations were beyond the scope of this work and will most likely be investigated in the future.

Conclusions

This work focused on the design and optimisation of 3D polymer-based photonic devices for light coupling, splitting, and environmental sensing and the possibility of integrating the plasmonic structure into two material platforms.

The work presents the process of designing and optimising two 3D MMI splitters made from IP-Dip polymer and fabricated using the DLW technique. Two designs were proposed, one with a 1×4 splitting ratio and the other with a 1×9 splitting ration. The design process satisfied the technological limitations, mainly the maximum length of 300 µm achievable in a single fabrication step. The BPM simulation showed minimal insertion loss and a wideband operation window for both designed MMI splitters. The designed structures were subsequently fabricated and characterised by the team from the University of Žilina. The NSOM measured power distribution at the output of each MMI showed that the power distribution was mainly retained with a bias toward one corner of the MMI. Investigation of possible reasons for this nonuniformity showed that axial misalignment of the structure against the fibre is the most likely culprit of this undesired phenomenon. The proposed solution for this predicament is a longer input waveguide to stabilise the propagating mode. An additional fabrication step would be needed to realise this optimisation, thus requiring further research beyond this work's scope.

Further, the work presents the analysis, simulation, and optimisation of 3D Fabry-Pérot interferometers at the tip of a single-mode fibre. The initial measurements showed that the structures' dimensions were in line with the design specifications provided by the University of Žilina. The further spectral measurements showed reflectance characteristics typical of dual-resonator devices, where intermodulation of the resonators caused an additional set of spectral peaks. Several simulation models were prepared based on the initial measurements, with the RCWA model being the most suitable for accuracy and computational demands. Subsequent simulations showed that the presence of the second resonator results in a reduced overall sensitivity of the device to environmental changes. The proposed optimisations included adjustments to the length of the second resonator and an introduction of a scattering structure at the end of the device. Both optimisations reduced the second resonator's contribution, thus reducing the undesired intermodulation. Another approach explored in this chapter was the interpretation of the spectral results using FFT. The so-called spatial spectrum provided information on changes within the device through changing phase values. The spatial spectrum interpretation was used to evaluate the environmental change characteristics obtained by the VSB Ostrava team. The results showed that the phase values closely followed the peak shift values. Furthermore, the results indicate that material expansion significantly affects the overall spectral shift introduced by the temperature and pressure change. In the case of temperature variation, the measurements' lower linearity suggests another influence besides the change in optical length. This change was attributed to the thermo-optic effect of IP-Dip.

The work also explored the viability of IP-Dip and SiON materials to support surface plasmon formation and propagation. The introduction of surface roughness showed

higher transmittance values and lower plasmon confinement. The roughness is a product of the DLW fabrication method specific to IP-Dip and cannot be avoided. This and the lack of means to procure samples needed for further investigation ruled out the IP-Dip material platform as a suitable candidate for a possible plasmonic-photonic device. The SiON material platform was also investigated regarding SPP compatibility since the technological process was available at ÚEF FEI STU at the time of writing. The samples acquired after the PECVD deposition step and ICP-RIE etching were measured using AFM to acquire surface roughness profiles for simulations. The tested parameters did not increase surface roughness in a way that would significantly influence SPP formation. The SiON thin film samples were also experimentally tested using ellipsometry, which confirmed the accuracy of simulation models. This makes the SiON platform suitable for Kretschmann configuration measurements. Further research into the effects of surface roughness on SPP formation was beyond the scope of this work. However, investigating the roughness after the metal mask removal step would benefit an accurate viability evaluation of SPP-supporting channel waveguide devices, the research topic of choice at ÚEF FEI STU.

Main Contributions of Dissertation Thesis
Related to Defined Objectives

1. The extent of existing research was reviewed, and the knowledge obtained was applied to further the understanding of polymer-based photonic and plasmonic-based devices in terms of design and simulation.

2. The limits of each used fabrication method were identified, and the limitations were accounted for in the simulation model formulation. In the case of 3D MMI splitters, the simulations showed a need for a single-step process. In 3D Fabry-Pérot interferometer—based sensors, the device's dimensions were modified according to the limitations of the DLW process. The surface characteristics obtained from measurements for plasmonic-photonic device evaluation provided further insight into the SiON fabrication process at ÚEF FEI STU.

3. Two 3D MMI splitter devices were designed and optimised for the desired splitting ratios, and available characterisation means. Their function was verified experimentally. Further optimisations of the devices were proposed to eliminate the undesired effects observed in measurements. 3D Fabry-Pérot interferometer-based sensors were characterised by available means. The acquired measurement results provided data for appropriate simulation model formulation. The simulation models provided further insight into the phenomena taking place and showed possible avenues of optimisation, for which new designs were proposed. A result interpretation method that allowed investigation of multi-resonator structures was implemented, resulting in new knowledge on the device's behaviour in the presence of environmental changes.

4. Two material platforms were evaluated regarding plasmonic structure integration. A simulation model that enables surface roughness modelling was created. One of these platforms proved to be a promising candidate for plasmonic-photonic devices.

5. The devices mentioned above and their simulation models were formulated based on extensive measurements of their spatial dimensions, surface roughness, spectral, and power characteristics. These measurements were realised using numerous methods such as spectrometry, SEM microscopy, optical microscopy, and AFM microscopy.

Resumé

Integrácia celofotonického spracovania dát naráža na limity v rámci materiálových základov. Najviac rozšírené fotonické čipy na báze kremíku nie sú zo svojej fyzikálnej podstaty (nepriamy polovodič) schopné spĺňať funkciu zdroja žiarenia. Táto nevýhoda je v súčasnosti riešená rôznymi formami hybridnej a heterogénnej integrácie iných materiálov na kremíkový čip. Takáto forma integrácie je limitovaná konvenčnou substraktívnou technológiou vytvárania vzorov. V porovnaní s ňou umožňujú polymérne materiály využitie aditívnych metód ako priame laserové popisovanie (direct laser writing, DLW). Takáto aditívna metóda výrazne zvyšuje flexibilitu návrhu, najmä vďaka možnosti lepšieho využitia tretieho priestorového rozmeru. Ďalšou perspektívnou oblasťou z hľadiska možnosti spoločnej integrácie je plazmonika. Kombináciou fotonických prvkov s plazmonickými štruktúrami je možné zlepšiť vlastnosti v rámci naviazania a snímania fyzikálnych vplyvov. Kombinovanie plazmonických štruktúr s fotonikou tiež do istej miery zmierňuje hlavnú nevýhodu plazmoniky, ktorou je vysoký útlm pri šírení.

Táto práca sa zameriava na návrh a optimalizáciu 3D polymérnych fotonických štruktúr pripravených pomocou DLW tlače. Polymérne štruktúry boli pripravené v spolupráci so Žilinskou univerzitou v Žiline. Práca sa tiež venuje vyšetreniu materiálových platforiem z hľadiska možnej integrácie plazmonických štruktúr.

Časť práce je venovaná návrhu a optimalizácii dvoch 3D deličov výkonu vytvorených z materiálu IP-Dip pomocou technológie DLW. Deliaci princíp využívaný pri oboch deličoch je multimódový interferenčný člen (multimode interference coupler, MMI). Návrh spočíval v simulácii správnych geometrických parametrov MMI členov pre zabezpečenie želaných deliacich pomerov (1×4 a 1×9). Vstupom do deliča bol mód jedno-módového optického vlákna (single mode fibre, SMF) s priemerom ~9 μm. Pre účely návrhu bol vytvorený 3D simulačný model využívajúci metódu šíriaceho sa lúča (Beam Propagation Method, BPM). Pred MMI člen bol v oboch deličoch umiestnený postupne zužujúci sa vstupný vlnovod. Vlnovod mal na vstupe priemer 10 μm (o 1 μm viac ako priemer vstupného módu žiarenia), kvôli citlivosti MMI na presné umiestnenie vstupného žiarenia. Z rovnakého dôvodu musel byť vstupný vlnovod vytvorený v jednom technologickom kroku. Tlač MMI a vstupného vlnovodu v dvoch krokoch a ich následné spojenie by mohlo viesť k nedokonalému prechodu medzi vstupným vlnovodom a MMI, čo by zmenilo povahu šírenia žiarenia v MMI člene a malo za následok nepredvídateľný tvar výstupného módového poľa. V rámci jedného kroku DLW tlače je možné vytvoriť maximálne 300 μm materiálu v osi Z. Tento limit teda určil maximálnu dĺžku celého deliča výkonu pre oba deliace pomery. Optimálne dĺžky MMI členov pre správny deliaci pomer boli 162 μm v prípade deliča 1×4 a 225 μm v prípade deliča 1×9. Následne boli vykonané spektrálne simulácie oboch deličov v rozsahu vlnových dĺžok využívaných pre optickú komunikáciu. Správna funkcia deličov bola zachovaná po hranicu 1400 nm a v prípade deliča 1×4 až po 1120 nm. Príprava štruktúr a ich následná charakterizácia pomocou NSOM (angl. near-field scanning microscopy) bola realizovaná Žilinskou univerzitou v Žiline. K navrhnutým deličom bola pridaná podporná štruktúra s vláknovou zásuvkou. Výsledky

merania rozloženia výstupného výkonu ukázali tvar poľa, ktoré bolo vo veľkej miere zhodné so simuláciami, a tiež nízke hodnoty vložných strát. Úrovne jednotlivých obrazov výstupného poľa vykazovali sklon voči jednému z rohov MMI v oboch meraných deličoch. Následne boli identifikované tri možné príčiny tejto nežiadúcej odchýlky: nadmerný ohyb vstupného vlákna, posun módu na vstupe MMI člena a nesprávne axiálne zarovnanie deliča voči stredovej osi vlákna. Každá z nich bola simulačne modelovaná pomocou BPM. Posledná vyšetrovaná príčina (nesprávne axiálne zarovnanie vlákna) mohla byť spôsobená buď deformáciou celej štruktúry, alebo nepresným uhlom čela vlákna voči vstupu deliča po zasunutí do vláknovej zásuvky. Simulácie nesprávneho axiálneho zarovnania vlákna ukázali podobný sklon výkonovej charakteristiky ako bol meraný. Snímka z optického mikroskopu tiež potvrdila miernu odchýlku stredovej osi vlákna od stredovej osi deliča. Z týchto dôvodov bolo za najpravdepodobnejšiu príčinu sklonu výkonovej charakteristiky deličov určené nesprávne axiálne zarovnanie vlákna voči deliču.

Ďalšia časť práce sa zamerala na optimalizáciu a vyšetrovanie fyzikálnych dejov v rámci pripravených 3D senzorov na báze Fabry-Pérotovho interferometra (FPI). Tieto senzory boli vytvorené z polyméru IP-Dip pomocou DLW a pozostávali z troch sekcií. Pomocou počiatočných meraní v podobe optickej a elektrónovej mikroskopie (scanning electron microscopy, SEM) boli overené rozmery dostupných FPI vzoriek. Tieto Spektrálne merania vložných strát v infračervenej časti spektra pri izbovej teplote ukázali prítomnosť dvoch sérii interferenčných maxím. Každá séria zodpovedala odozve jedného z dvoch rezonátorov prítomných v štruktúre FPI súčiastky. Prvý rezonátor bol tvorený vzduchovou dutinou medzi dvoma sekciami IP-Dip polyméru, druhým rezonátorom bola vrstva IP-Dip, ktorá slúžila pre odraz od konca vyšetrovanej štruktúry. Na základe vyššie spomenutých meraní boli navrhnuté tri simulačné modely pre tri simulačné metódy. Pre ďalšie simulácie bola zvolená metóda rigorózna analýza viazaných vĺn (Rigorous Coupled-Wave Analysis, RCWA) pre relatívne nízke výpočtové nároky. Simulované spektrálne charakteristiky pri zmene vybraných parametrov (index lomu vzduchovej dutiny, dĺžka vzduchovej dutiny) poskytli maximálny merateľný rozsah a hodnoty senzitivity merania daných parametrov. Senzitivita pôvodného návrhu senzora bola vo výsledkoch simulácii polovičná v porovnaní s ideálnou štruktúrou. Simuláciou jednotlivých rezonátorov bola následne potvrdená vzájomná interferencia medzi dvoma rezonátormi v pôvodnom návrh FPI senzora. Na základe predošlých simulácii boli vytvorené návrhy optimalizovaných senzorov s cieľom odstránenia nežiaduceho vplyvu polymérneho rezonátora. Prvá optimalizácia spočívala v redukcii dĺžky polymérneho rezonátora na 5,4 µm, čo vytvorilo spektrálne okno s minimalizovaným nežiaducim vplyvom v okolí vlnovej dĺžky 1580 nm. Ďalšou navrhnutou optimalizáciou bolo umiestnenie periodickej štruktúry na koniec senzora, ktorá by zabezpečila útlm spätného odrazu od posledného rozhrania štruktúry. Podobné riešenie bolo aj experimentálne overené v dostupnej literatúre. Pri spracovaní výsledkov meraní a simulácii bolo uplatnené dodatočné spracovanie pomocou algoritmu rýchlej Fourierovej transformácie (Fast Fourier Transform, FFT). Tento prístup umožnil kvantifikovať zmeny v meraných charakteristikách na základe hodnôt fázového posunu Výsledky simulovaných zmien parametrov senzorov ukázali lineárnu zmenu hodnôt fázového posunu

v optimalizovanom senzore s krátkym polymérnym rezonátorom. V prípade pôvodného návrhu zmena fázy nebola lineárna z dôvodu blízkosti rezonančných frekvencií dvoch prítomných rezonátorov. Napriek tomu bolo pri každom testovanom návrhu možné priradiť hodnoty fázy k hodnotám simulovaných parametrov. Následne boli pomocou popísaného postupu určené hodnoty dĺžky vzduchovej dutiny, ktoré zodpovedali nameraným hodnotám v rámci možnej chyby. Na základe meraných rozmerov pripravených senzorov boli tiež určené približné hodnoty indexu lomu materiálu IP-Dip vyplývajúce z termo-optického koeficientu. Súčasťou kapitoly sú tiež spracované merania zmien tlaku a teploty okolitého prostredia realizované v spolupráci s Vysokou školou báňskou – Technická univerzita Ostrava. Vzorky použité pri meraniach pochádzali z inej série ako vzorky z počiatočných meraní na ÚEF FEI STU. Zo spektrálnych charakteristík boli nadobudnuté hodnoty pozícii interferenčných maxím a hodnoty FFT fázových posunov. Hodnoty fázových posunov boli porovnané s výsledkami simulácií. Týmto postupom boli odčítané dĺžky vzduchových dutín každej vzorky. Fázové posuny korelovali so simuláciami zmeny dĺžky. Odchýlky od simulovaných charakteristík v prípade zmeny teploty boli pripísané k vplyvu termo-optického efektu. Celkovo metóda interpretácie výsledkov pomocou hodnoty FFT fázových posunov umožnila prepojenie simulovaných charakteristík s meranými.

Práca sa tiež zaoberala prepojením plazmonických štruktúr s dvoma materiálovými základmi. Prvým testovaným materiálovým základom bol polymér IP-Dip pripravený pomocou DLW tlače. Druhým testovaným materiálom bol oxynitrid kremíka (SiON), pripravený pomocou technologického procesu dostupného na ÚEF FEI STU. V prípade polyméru bol najprv vytvorený model využívajúci metódu FDTD. Pomocou tohto modelu bola verifikovaná kompatibilita materiálu IP-Dip s plynnými analytmi. Model potvrdil vybudenie povrchového plazmónu (Surface Plasmon Polariton, SPP) pri vlnovej dĺžke 720 nm a uhle dopadu 43,6. Následne bol vytvorený model pre metódu konečných prvkov (Finite Element Method, FEM), ktorý umožnil implementáciu drsného povrchu získaného pomocou mikroskopie atómových síl (Atomic Force Microscopy, AFM). Krivky reprezentujúce povrch polyméru IP-Dip pochádzali z dostupnej literatúry. Testovaný analyt bol v tomto prípade zmenený na vodný roztok a excitačná vlnová dĺžka na 632 nm. Výsledky simulácií drsných povrchov IP-Dip vykazovali zvýšené hodnoty transmitancie a útlm optického výkonu naviazaného do plazmónu. Plazmonická rezonancia bola v charakteristikách napriek tomu zreteľná, aj keď v značne skreslenej forme. Je potrebné dodať, že aproximácie použité vo FEM modeli (2D simulácia a dokonale rovnomerná zlatá vrstva) s najväčšou pravdepodobnosťou kladne prispeli k šíreniu povrchového plazmónu v simulačnej doméne. Realizácia prvku s potrebným incidenčným uhlom 70° by zrejme tiež zvýraznila zvlnenie povrchu charakteristické pre DLW tlač. Kvoli nedostupnosti potrebnej technológie bol ďalší výskum týkajúci sa hybridného fotonicky-plazmonického prvku mimo rozsah tejto práce. Ako ďalší materiálový základ bol testovaný SiON, najmä vďaka dostupnosti technológie a vysokej úrovni jeho doterajšieho výskumu na ÚEF FEI STU. Tenké vrstvy SiON boli merané pomocou AFM v dvoch fázach zavedeného technologického procesu fabrikácie vlnovodných štruktúr. Prvá séria AFM meraní bola realizovaná po počiatočnej depozícii tenkých vrstiev pomocou plazmatického nanášania

odparovaním (Plasma-enhanced Chemical Vapour Deposition, PECVD). Žiadny z testovaných parametrov sa vo výraznej miere neprejavil v zmene štatistických veličín drsnosti, ktoré dosahovali priemrnú drsnosť. Excitačná vlnová dĺžka sa vo všetkých simuláciách výrazne nevzdialila od hodnoty 630 nm. Hodnota rezonančného uhla bola 68,4°. Druhá séria AFM meraní bola realizovaná po leptaní prostredníctvom technológie reaktívneho iónového leptania (Inductively Coupled Plasma – Reactive Ion Etching, ICP-RIE). Testované vzorky boli vystavené rôznym časom leptania. Oproti vzorkám po kroku PECVD sa priemerná drsnosť materiálu zvýšila o 1 nm (časy leptania 3 a 6 min.). Väčšia odchýlka v rámci drsnosti nastala pri čase leptania 12 min. kde hodnota priemernej drsnosti vzrástla na ~10 nm. Povrch s touto zvýšenou mierou drsnosti vykazoval zvýšené hodnoty transmitancie v simulovaných charakteristikách. Všetky testované série vzoriek umožňovali v simulácii vybudenie SPP a jeho šírenie s minimálnou odchýlkou voči ideálne hladkému povrchu. Tenké vrstvy SiON bez ďalšieho tvarovania boli tiež použité pri experimentálnom vybudení SPP v Kretschmannovej konfigurácii pomocou elipsometrie. Simulácie týchto štruktúr tenkých vrstiev vykazovali uhol a vlnovú dĺžku excitácie s minimálnou odchýlkou voči experimentálne určeným hodnotám. Toto do istej miery potvrdzuje schopnosť použitého FEM modelu verne simulovať prítomné plazmonické javy. Pre použitie SiON vrstiev vo vlnovodných senzoroch s využitím plazmonických efektov je potrebné vykonať merania drsnosti povrchov a simulácie ich vplyvu na SPP v ostatných krokoch technologického procesu. Tieto merania budú predmetom ďalšieho výskumu.

References

1. CAIMI, Daniele et al. Heterogeneous Integration of III–V Materials by Direct Wafer Bonding for High-Performance Electronics and Optoelectronics. *IEEE Transactions on Electron Devices*. July 2021. Vol. 68, no. 7, p. 3149–3156. DOI 10.1109/TED.2021.3067273.

2. KAUR, Paramjeet et al. Hybrid and heterogeneous photonic integration. *APL Photonics*. 28 June 2021. Vol. 6, no. 6, p. 061102. DOI 10.1063/5.0052700.

3. GAO, Hongwei et al. 3D printed optics and photonics: Processes, materials and applications. *Materials Today*. 1 October 2023. Vol. 69, p. 107–132. DOI 10.1016/j.mattod.2023.06.019.

4. S, Parvathi Nair et al. 3D printed fiber sockets for plug and play micro-optics. *International Journal of Extreme Manufacturing*. November 2020. Vol. 3, no. 1, p. 015301. DOI 10.1088/2631-7990/abc674.

5. BERWIND, M. F. et al. Rapidly prototyping biocompatible surfaces with designed wetting properties via photolithography and plasma polymerization. *Microfluidics and Nanofluidics*. 17 August 2017. Vol. 21, no. 9, p. 144. DOI 10.1007/s10404-017-1984-6.

6. DENG, Qingzhong et al. Arbitrary-ratio 1 × 2 power splitter based on asymmetric multi-mode interference. *Optics Letters*. 1 October 2014. Vol. 39, no. 19, p. 5590–5593. DOI 10.1364/OL.39.005590.

7. ZHONG, Wanqin and XIAO, Jinbiao. Ultracompact polarization-insensitive power splitter using subwavelength-grating-based MMI couplers on an SOI platform. *Applied Optics*. 1 March 2020. Vol. 59, no. 7, p. 1991–1997. DOI 10.1364/AO.382097.

8. YIN, Mei et al. CMOS-compatible and fabrication-tolerant MMI-based polarization beam splitter. *Optics Communications*. 15 January 2015. Vol. 335, p. 48–52. DOI 10.1016/j.optcom.2014.08.060.

9. KIM, Seong-Hwan et al. High-Performance Silicon MMI Switch Based on Thermo-Optic Control of Interference Modes. *IEEE Photonics Technology Letters*. August 2018. Vol. 30, no. 16, p. 1427–1430. DOI 10.1109/LPT.2018.2850907.

10. CHENG, Ru et al. Fluorinated photopolymer cascaded MMI-based integrated optical waveguide switching matrix with encoding functions. *Optics Express*. 29 April 2019. Vol. 27, no. 9, p. 12883–12898. DOI 10.1364/OE.27.012883.

11. KUDALIPPALLIYALIL, Ramesh et al. Low-loss and ultra-broadband silicon nitride angled MMI polarization splitter/combiner. *Optics Express*. 9 November 2020. Vol. 28, no. 23, p. 34111–34122. DOI 10.1364/OE.405188.

12. MOHAMMED, Zakriya et al. An Ultra-Compact CMOS Compatible MMI based 1310/1550 nm Wavelength (de) Multiplexer. In : *2021 European Conference on Optical Communication (ECOC)*. September 2021. p. 1–3. DOI 10.1109/ECOC52684.2021.9606089.

13. GUO, Fei et al. An MMI-Based Mode (DE)MUX by Varying the Waveguide Thickness of the Phase Shifter. *IEEE Photonics Technology Letters*. November 2016. Vol. 28, no. 21, p. 2443–2446. DOI 10.1109/LPT.2016.2599934.

14. Y. ELSAYED, Mohamed et al. Integrated Lab-on-a-Chip Optical Biosensor Using Ultrathin Silicon Waveguide SOI MMI Device. *Sensors*. January 2020. Vol. 20, no. 17, p. 4955. DOI 10.3390/s20174955.

15. SOURES, Nicholas et al. Neuro-MMI: A Hybrid Photonic-Electronic Machine Learning Platform. In : *2018 IEEE Photonics Society Summer Topical Meeting Series (SUM)*. July 2018. p. 187–188. DOI 10.1109/PHOSST.2018.8456766.

16. SOLDANO, L.B. and PENNINGS, E.C.M. Optical multi-mode interference devices based on self-imaging: principles and applications. *Journal of Lightwave Technology*. April 1995. Vol. 13, no. 4, p. 615–627. DOI 10.1109/50.372474.

17. SCHMID, Michael, LUDESCHER, Dominik and GIESSEN, Harald. Optical properties of photoresists for femtosecond 3D printing: refractive index, extinction, luminescence-dose dependence, aging, heat treatment and comparison between 1-photon and 2-photon exposure. *Optical Materials Express*. 1 December 2019. Vol. 9, no. 12, p. 4564–4577. DOI 10.1364/OME.9.004564.

18. MIZERA, Tomas et al. 3D Polymer-Based 1 × 4 MMI Splitter. *Nanomaterials*. January 2022. Vol. 12, no. 10, p. 1749. DOI 10.3390/nano12101749.

19. MIZERA, Tomáš. *3D fotonické prvky pre aplikácie na čipe*. . Žilina : Žilinská univerzita v Žiline, Fakulta elektrotechniky a informačných technológií, 2022. 271123-UK/Z

20. ZHU, Chen et al. Advances in Fiber-Optic Extrinsic Fabry–Perot Interferometric Physical and Mechanical Sensors: A Review. *IEEE Sensors Journal*. April 2023. Vol. 23, no. 7, p. 6406–6426. DOI 10.1109/JSEN.2023.3244820.

21. SAAVEDRA, Carlos et al. Spectroscopic Gas Sensor Based on a Fiber Fabry-Perot Cavity. *Physical Review Applied*. 17 October 2022. Vol. 18, no. 4, p. 044039. DOI 10.1103/PhysRevApplied.18.044039.

22. WILLIAMS, Jeremiah et al. Optical Fiber-Tip Heat Sensor Featuring a Multipositional Fabry–Pérot Cavity Resonator. In : *2020 IEEE SENSORS*. Online. October 2020. p. 1–4. [Accessed 21 April 2024]. DOI 10.1109/SENSORS47125.2020.9278730.

23. ZHANG, Dengwei et al. Highly sensitive magnetic field microsensor based on direct laser writing of fiber-tip optofluidic Fabry–Pérot cavity. *APL Photonics*. July 2020. Vol. 5, no. 7, p. 076112. DOI 10.1063/5.0012988.

24. MACLEOD, H. A. *Thin-film optical filters*. . 3rd ed. Bristol ; Philadelphia : Institute of Physics Pub, 2001. ISBN 978-0-7503-0688-1. QC373.L5 M34 2001

25. Fabry-Perot Interferometer. Online. [Accessed 22 March 2024]. Available from: http://www.physicsbootcamp.org/section-fabry-perot-interferometer.html

26.	LIAO, C. R., HU, T. Y. and WANG, D. N. Optical fiber Fabry-Perot interferometer cavity fabricated by femtosecond laser micromachining and fusion splicing for refractive index sensing. *Optics Express*. 24 September 2012. Vol. 20, no. 20, p. 22813–22818. DOI 10.1364/OE.20.022813.

27.	SMITH, Jonathan W et al. Three-dimensional Fabry–Pérot cavities sculpted on fiber tips using a multiphoton polymerization process. *Journal of Micromechanics and Microengineering*. 1 December 2020. Vol. 30, no. 12, p. 125007. DOI 10.1088/1361-6439/abc0fd.

28.	GORAUS, Matej et al. Polymer lab-on-fiber probe based on Fabry-Perot resonator. In : *2020 ELEKTRO*. Online. Taormina, Italy : IEEE, May 2020. p. 1–4. [Accessed 12 June 2023].	ISBN 978-1-72817-542-3. DOI 10.1109/ELEKTRO49696.2020.9130195.

29.	MENON, P Susthitha et al. Urea and creatinine detection on nano-laminated gold thin film using Kretschmann-based surface plasmon resonance biosensor. *PLOS ONE*. 27 July 2018. Vol. 13, p. e0201228. DOI 10.1371/journal.pone.0201228.

30.	FREI, Walter. How to Model the Optical Properties of Rough Surfaces. *COMSOL*. Online.	[Accessed 9 April 2024].	Available	from: https://www.comsol.com/blogs/how-to-model-the-optical-properties-of-rough-surfaces/

31.	OCIER, Christian R. et al. Direct laser writing of volumetric gradient index lenses and waveguides. *Light: Science & Applications*. 3 December 2020. Vol. 9, no. 1, p. 196. DOI 10.1038/s41377-020-00431-3.

32.	JOHNSON, P. B. and CHRISTY, R. W. Optical Constants of the Noble Metals. *Physical Review B*. 15 December 1972. Vol. 6, no. 12, p. 4370–4379. DOI 10.1103/PhysRevB.6.4370.

33.	FEILER, Martin et al. Design of Optimal SPR-Based Multi-mode Waveguide Sensor for a Wide Range of Liquid Analytes. *Photonics*. June 2023. Vol. 10, no. 6, p. 618. DOI 10.3390/photonics10060618.

34.	CHLPÍK, Juraj et al. Total internal reflection ellipsometry of Au/SiOxNy waveguide structures for sensor applications. *AIP Conference Proceedings*. 5 May 2023. Vol. 2778, no. 1, p. 030005. DOI 10.1063/5.0135889.

Zoznam publikačnej činnosti autora

1. Výstupy kategórie A+, A, A- a B, spolu: 21
2. Výstupy kategórie A+ a A, spolu: 3
3. Počet publikácii vo WoS/SCOPUS: 7 (z toho 5 WoS a 7 SCOPUS)

Kategória A+: 3

V3 Vedecký výstup publikačnej činnosti z časopisu

V3_01   FEILER, Martin [65 %] - **ZIMAN, Martin** [15 %] - KOVÁČ, Jaroslav jr. [10 %] - KUZMA, Anton [5 %] - UHEREK, František [5 %]. Design of Optimal SPR-Based Multimode Waveguide Sensor for a Wide Range of Liquid Analytes. In *Photonics*. Vol. 10, iss. 6 (2023), Art. no. 618 [10] s. ISSN 2304-6732 (2022: 2.400 - IF, Q3 - JCR Best Q, 0.479 - SJR, Q2 - SJR Best Q). V databáze: DOI: 10.3390/photonics10060618 ; WOS: 001017896200001 ; CC: 001017896200001 ; SCOPUS: 2-s2.0-85163794308. Typ výstupu: článok; Výstup: zahraničný; Kategória publikácie do 2021: ADC

V3_02   MIZERA, Tomáš [35 %] - GAŠO, Peter [20 %] - PUDIŠ, Dušan [15 %] - **ZIMAN, Martin** [20 %] - KUZMA, Anton [5 %] - GORAUS, Matej [5 %]. 3D polymer-based 1 × 4 MMI splitter. In *Nanomaterials*. Vol. 12, iss. 10 (2022), Art. no. 1749 [10] s. ISSN 2079-4991 (2022: 5.300 - IF, Q1 - JCR Best Q, 0.811 - SJR, Q1 - SJR Best Q). V databáze: SCOPUS: 2-s2.0-85130365130 ; WOS: 000802495600001 ; CC: 000802495600001 ; DOI: 10.3390/nano12101749. Typ výstupu: článok; Výstup: zahraničný; Kategória publikácie do 2021: ADC

V3_03   **ZIMAN, Martin** [55 %] - FEILER, Martin [15 %] - MIZERA, Tomáš [15 %] - KUZMA, Anton [5 %] - PUDIŠ, Dušan [5 %] - UHEREK, František [5 %]. Design of a power splitter based on a 3D MMI coupler at the fibre-tip. In *Electronics*. Vol. 11, iss. 18 (2022), Art. no. 2815 [11] s. ISSN 2079-9292 (2022: 2.900 - IF, Q2 - JCR Best Q, 0.628 - SJR, Q2 - SJR Best Q). V databáze: DOI: 10.3390/electronics11182815 ; SCOPUS: 2-s2.0-85138694363 ; WOS: 000856492300001 ; CC: 000856492300001. Typ výstupu: článok; Výstup: zahraničný; Kategória publikácie do 2021: ADC

Kategória A-: 5

V2 Vedecký výstup publikačnej činnosti ako časť editovanej knihy alebo zborníka

V2_01   GAŠO, Peter [40 %] - MIZERA, Tomáš [40 %] - PUDIŠ, Dušan [10 %] - **ZIMAN, Martin** [5 %] - JANDURA, Daniel [5 %]. 1 x 9 MMI splitter prepared by 3D lithography and characterized by NSOM. In *22nd Polish-Slovak-Czech Optical Conference on Wave and Quantum Aspects of Contemporary Optics : Wojanow, Poland. September 5-9, 2022*. Bellingham : SPIE, 2022, Art. no. 125020Q [5] s. ISSN 0277-786X. ISBN 978-1-510-66111-0 (2022: 0.166 - SJR). V databáze: DOI: 10.1117/12.2664185 ; SCOPUS: 2-s2.0-85145348529 ; WOS: 000920988700025. Typ výstupu: príspevok z podujatia; Výstup: zahraničný; Kategória publikácie do 2021: AFC

V2_02   CHLPÍK, Juraj [25 %] - KOVÁČOVÁ, Soňa [10 %] - PODLUCKÝ, ¼uboš [10 %] -
         ZIMAN, Martin [10 %] - FEILER, Martin [10 %] - KOTOROVÁ, Soňa [10 %] -
         KOVÁČ, Jaroslav jr. [10 %] - VÁRY, Tomáš [10 %] - CIRÁK, Július [5 %]. Total
         internal reflection ellipsometry of Au/SiOxNy waveguide structures for sensor
         applications. In *APCOM 2022 : 27th International conference on applied physics of
         condensed matter. Štrbské Pleso, Slovak Republic. June 22-24, 2022*. 1. ed. Melville :
         AIP Publishing, 2023, Art. no. 030005 [7] s. ISSN 0094-243X. ISBN 978-0-7354-4479-
         9 (2022: 0.164 - SJR). V databáze: DOI: 10.1063/5.0135889 ; SCOPUS: 2-s2.0-
         85160269603   ;   WOS: 001055613400026.
         Typ výstupu: príspevok z podujatia; Výstup: domáci; Kategória publikácie do 2021:
         AFD

V2_03   LETTRICHOVÁ, Ivana [27 %] - PUDIŠ, Dušan [20 %] - JANDURA, Daniel [15 %] -
         GAŠO, Peter [10 %] - FEILER, Martin [10 %] - KOVÁČ, Jaroslav jr. [10 %] -
         LAURENČÍKOVÁ, Agáta [5 %] - **ZIMAN, Martin** [3 %]. IP-Dip inverted pyramids
         for application in SERS. In *22nd Polish-Slovak-Czech Optical Conference on Wave and
         Quantum Aspects of Contemporary Optics : Wojanow, Poland. September 5-9, 2022*.
         Bellingham : SPIE, 2022, Art. no. 125020P [6] s. ISSN 0277-786X. ISBN 978-1-510-
         66111-0 (2022: 0.166 - SJR). V databáze: DOI: 10.1117/12.2664208 ; SCOPUS: 2-s2.0-
         85145359283   ;   WOS: 000920988700024.
         Typ výstupu: príspevok z podujatia; Výstup: zahraničný; Kategória publikácie do 2021:
         AFC

V2_04   PUDIŠ, Dušan [25 %] - MIZERA, Tomáš [20 %] - GAŠO, Peter [15 %] - KUZMA,
         Anton [10 %] - **ZIMAN, Martin** [10 %] - SEREČUNOVÁ, Stanislava [10 %] -
         SEYRINGER, Dana [5 %] - GORAUS, Matej [5 %]. 3D optical splitters based on
         polymers. In *ASDAM 2022 : 14th International conference on advanced semiconductor
         devices and microsystems. Smolenice, Slovakia. October 23-26, 2022*. 1. ed. Danvers :
         IEEE, 2022, S. 45-48. ISBN 978-1-6654-6977-7. V databáze: DOI:
         10.1109/ASDAM55965.2022.9966741 ; IEEE: 9966741 ; SCOPUS: 2-s2.0-
         85144592537.
         Typ výstupu: príspevok z podujatia; Výstup: domáci; Kategória publikácie do 2021:
         AFD

V2_05   PUDIŠ, Dušan [30 %] - MIZERA, Tomáš [25 %] - GAŠO, Peter [20 %] - **ZIMAN,
         Martin** [10 %] - SEREČUNOVÁ, Stanislava [10 %] - SEYRINGER, Dana [5 %]. 3D
         MMI optical splitter with output waveguides and its near-field characterization. In *22nd
         Polish-Slovak-Czech Optical Conference on Wave and Quantum Aspects of
         Contemporary Optics : Wojanow, Poland. September 5-9, 2022*. Bellingham : SPIE,
         2022, Art. no. 125020O [5] s. ISSN 0277-786X. ISBN 978-1-510-66111-0 (2022: 0.166
         - SJR). V databáze: DOI: 10.1117/12.2664188 ; SCOPUS: 2-s2.0-85145349654 ; WOS:
         000920988700023.
         Typ výstupu: príspevok z podujatia; Výstup: zahraničný; Kategória publikácie do 2021:
         AFC

Kategória B: 13

V2 Vedecký výstup publikačnej činnosti ako časť editovanej knihy alebo zborníka

V2_06   FEILER, Martin [50 %] - **ZIMAN, Martin** [15 %] - KUZMA, Anton [15 %] - KOVÁČ, Jaroslav jr. [10 %] - UHEREK, František [10 %]. Design and simulation of optical waveguide sensor based on SiN material platform utilising surface plasmon resonance. In *ADEPT 2021 : 9th International conference on advances in electronic and photonic technologies. Podbanské, Slovakia. September 20-23.2021*. 1. vyd. Žilina : Vydavateľstvo EDIS, 2021, S. 95-98. ISBN 978-80-554-1806-3. Výstup: domáci; Kategória publikácie do 2021: AFD

V2_07   FEILER, Martin [65 %] - **ZIMAN, Martin** [20 %] - KUZMA, Anton [5 %] - KOVÁČ, Jaroslav jr. [5 %] - UHEREK, František [5 %]. Design and simulation of optical grating coupler on SiON material platform. In *ELITECH´22 [elektronický zdroj] : 24th Conference of Doctoral Students. Bratislava, Slovakia. June 1, 2022*. 1. ed. Bratislava : Vydavateľstvo Spektrum STU, 2022, [4] s. ISBN 978-80-227-5192-6. Typ výstupu: príspevok z podujatia; Výstup: domáci; Kategória publikácie do 2021: AFD

V2_08   FEILER, Martin [60 %] - **ZIMAN, Martin** [15 %] - KUZMA, Anton [10 %] - KOVÁČ, Jaroslav jr. [10 %] - UHEREK, František [5 %]. Design and simulation of grating for fiber-to-chip coupling on SiON material platform. In *ADEPT 2022 : 10th International conference on advances in electronic and photonic technologies. Tatranská Lomnica, Slovakia. June 20-24, 2022*. 1. vyd. Žilina : Vydavateľstvo EDIS, 2022, S. 101-104. ISBN 978-80-554-1884-1.
Typ výstupu: príspevok z podujatia; Výstup: domáci; Kategória publikácie do 2021: AFD

V2_09   FEILER, Martin [65 %] - **ZIMAN, Martin** [15 %] - KOVÁČ, Jaroslav jr. [10 %] - KUZMA, Anton [10 %]. Single-mode waveguide based SPR refractive index sensor for lab-on-chip applications. In *ADEPT 2023 : 11th International conference on advances in electronic and photonic technologies. Podbanské, Slovakia. June 12-15, 2023*. 1. vyd. Žilina : Vydavateľstvo EDIS, 2023, S. 75-78. ISBN 978-80-554-1977-0.
Typ výstupu: príspevok z podujatia; Výstup: domáci; Kategória publikácie do 2021: AFD

V2_10   GAŠO, Peter [30 %] - MIZERA, Tomáš [30 %] - **ZIMAN, Martin** [20 %] - PUDIŠ, Dušan [10 %] - KUZMA, Anton [10 %]. Multi-mode interference splitter. In *ADEPT 2022 : 10th International conference on advances in electronic and photonic technologies. Tatranská Lomnica, Slovakia. June 20-24, 2022*. 1. vyd. Žilina : Vydavateľstvo EDIS, 2022, S. 177-180. ISBN 978-80-554-1884-1.
Typ výstupu: príspevok z podujatia; Výstup: domáci; Kategória publikácie do 2021: AFD

V2_11   CHOVAN, Jozef [20 %] - UHEREK, František [50 %] - HAŠKO, Daniel [5 %] - PODLUCKÝ, ¼uboš [10 %] - **ZIMAN, Martin** [5 %] - KOZA, Eduard [5 %] - PAVLOV, Jozef [5 %]. Active alignment system of fiber array coupling to photonics integrated circuits. In *ADEPT 2020 : 8th International conference on advances in*

electronic and photonic technologies. Nový Smokovec, Slovakia. September 14-17, 2020. 1. vyd. Žilina : Vydavateľstvo EDIS, 2020, S. 57-60. ISBN 978-80-554-1735-6. Kategória publikácie do 2021: AFD

V2_12　　MIZERA, Tomáš [30 %] - GAŠO, Peter [20 %] - PUDIŠ, Dušan [15 %] - **ZIMAN, Martin** [15 %] - KUZMA, Anton [15 %] - GORAUS, Matej [5 %]. Polymer based 3D 1x4 MMI splitter. In *ADEPT 2022 : 10th International conference on advances in electronic and photonic technologies. Tatranská Lomnica, Slovakia. June 20-24, 2022*. 1. vyd. Žilina : Vydavateľstvo EDIS, 2022, S. 109-112. ISBN 978-80-554-1884-1. Typ výstupu: príspevok z podujatia; Výstup: domáci; Kategória publikácie do 2021: AFD

V2_13　　**ZIMAN, Martin** [50 %] - CHOVAN, Jozef [20 %] - KUZMA, Anton [10 %] - UHEREK, František [10 %] - KOVÁČ, Jaroslav jr. [10 %]. Design of basic integrated photonic devices for use in optical communication systems. In *ADEPT 2020 : 8th International conference on advances in electronic and photonic technologies. Nový Smokovec, Slovakia. September 14-17, 2020*. 1. vyd. Žilina : Vydavateľstvo EDIS, 2020, S.　　　　　119-122.　　　　　ISBN　　　　　978-80-554-1735-6. Kategória publikácie do 2021: AFD

V2_14　　**ZIMAN, Martin** [50 %] - FEILER, Martin [15 %] - KUZMA, Anton [15 %] - KOVÁČ, Jaroslav jr. [10 %] - UHEREK, František [10 %]. Simulations of surface plasmon resonance based fiber probe. In *ADEPT 2021 : 9th International conference on advances in electronic and photonic technologies. Podbanské, Slovakia. September 20-23.2021*. 1. vyd. Žilina : Vydavateľstvo EDIS, 2021, S. 175-178. ISBN 978-80-554-1806-3. Výstup: domáci; Kategória publikácie do 2021: AFD

V2_15　　**ZIMAN, Martin** [40 %] - FEILER, Martin [15 %] - UHEREK, František [10 %] - MIZERA, Tomáš [15 %] - KUZMA, Anton [10 %] - JAGELKA, Martin [10 %]. Design and simulation of 3D MMI splitter based on polymer. In *ELITECH´22 [elektronický zdroj] : 24th Conference of Doctoral Students. Bratislava, Slovakia. June 1, 2022*. 1. ed. Bratislava : Vydavateľstvo Spektrum STU, 2022, [5] s. ISBN 978-80-227-5192-6. Typ výstupu: príspevok z podujatia; Výstup: domáci; Kategória publikácie do 2021: AFD

V2_16　　**ZIMAN, Martin** [60 %] - KUZMA, Anton [10 %] - FEILER, Martin [10 %] - MIZERA, Tomáš [10 %] - PUDIŠ, Dušan [5 %] - UHEREK, František [5 %]. Design and simulations of 1xN polymer-based MMI splitters. In *ADEPT 2022 : 10th International conference on advances in electronic and photonic technologies. Tatranská Lomnica, Slovakia. June 20-24, 2022*. 1. vyd. Žilina : Vydavateľstvo EDIS, 2022, S. 238-241. ISBN　　　　　　　　　　　　　　978-80-554-1884-1. Typ výstupu: príspevok z podujatia; Výstup: domáci; Kategória publikácie do 2021: AFD

V2_17　　**ZIMAN, Martin** [20 %] - FEILER, Martin [20 %] - MIZERA, Tomáš [20 %] - KUZMA, Anton [20 %] - UHEREK, František [20 %]. Návrh a simulácie deliča výkonu založeného na 3D MMI člene. In *Fotonika 2022 : 17. výročný vedecký seminár*

Medzinárodného laserového centra CVTI SR. Bratislava, Slovakia. 07. december 2022. Bratislava : Medzinárodné laserové centrum, 2022, S. 111-115. ISBN 978-80-8240-033-8.

Typ výstupu: príspevok z podujatia; Výstup: domáci; Kategória publikácie do 2021: AFD

V2_18   **ZIMAN, Martin** [60 %] - FEILER, Martin [15 %] - KOVÁČ, Jaroslav jr. [15 %] - DONOVAL, Daniel [5 %] - KUZMA, Anton [5 %]. Simulation investigation of fibre-tip sensor prepared by DLW printing. In *ADEPT 2023 : 11th International conference on advances in electronic and photonic technologies. Podbanské, Slovakia. June 12-15, 2023*. 1. vyd. Žilina : Vydavateľstvo EDIS, 2023, S. 123-126. ISBN 978-80-554-1977-0.

Typ výstupu: príspevok z podujatia; Výstup: domáci; Kategória publikácie do 2021: AFD

Ostatné publikácie: 1

V1 Vedecký výstup publikačnej činnosti ako celok

V1_01   FEILER, Martin [25 %] - (zost.) - **ZIMAN, Martin** [25 %] - (zost.) - KOVÁČOVÁ, Soňa [25 %] - (zost.) - KOVÁČ, Jaroslav jr. [25 %] - (zost.). *ADEPT 2022 : 10th International conference on advances in electronic and photonic technologies. Tatranská Lomnica, Slovakia. June 20-24, 2022*. 1. vyd. Žilina : Vydavateľstvo EDIS, 2022.   274   s.   ISBN   978-80-554-1884-1.

Typ výstupu: zborník; Výstup: domáci; Kategória publikácie do 2021: FAI

Štatistika: kategória publikačnej činnosti od 2022

V1	Vedecký výstup publikačnej činnosti ako celok	1
V2	Vedecký výstup publikačnej činnosti ako časť editovanej knihy alebo zborníka	18
V3	Vedecký výstup publikačnej činnosti z časopisu	3
Súčet		**22**

Štatistika: kategória publikačnej činnosti do 2021

ADC	Vedecké práce v zahraničných karentovaných časopisoch	3
AFC	Publikované príspevky na zahraničných vedeckých konferenciách	3
AFD	Publikované príspevky na domácich vedeckých konferenciách	15
FAI	Redakčné a zostavovateľské práce knižného charakteru (bibliografie, encyklopédie, katalógy, slovníky, zborníky...)	1
Súčet		**22**

Ohlasy na publikácie autora

Citácie, spolu: 4 (Z toho registrované vo WoS alebo SCOPUS: 4)

Publikácia:

MIZERA, Tomáš [35 %] - GAŠO, Peter [20 %] - PUDIŠ, Dušan [15 %] - **ZIMAN, Martin** [20 %] - KUZMA, Anton [5 %] - GORAUS, Matej [5 %]. 3D polymer-based 1×4 MMI splitter. In *Nanomaterials*. Vol. 12, iss. 10 (2022), Art. no. 1749 [10] s. ISSN 2079-4991 (2022: 5.300 - IF, Q1 - JCR Best Q, 0.811 - SJR, Q1 - SJR Best Q). V databáze: SCOPUS: 2-s2.0-85130365130 ; WOS: 000802495600001 ; CC: 000802495600001 ; DOI: 10.3390/nano12101749.
Typ výstupu: článok; Výstup: zahraničný; Kategória publikácie do 2021: ADC

Citovaná v:

SRIVASTAVA, Kritarth and BHATIA, Nitin. Design of all-fiber 2D MMI based optical devices using 1D mode propagation method. Optics Communications. 15 May 2024. Vol. 559, p. 130426. DOI 10.1016/j.optcom.2024.130426.

LI, Jiawei et al. Optical Waveguides Fabricated via Femtosecond Direct Laser Writing: Processes, Materials, and Devices. Advanced Materials Technologies. 2023. Vol. 8, no. 18, p. 2300620. DOI 10.1002/admt.202300620.

AI, Siwen et al. Ultrafast laser inscription of 2D confinement MMI-based beam splitters with tunable splitting ratio in Nd:YAG crystal. Optics & Laser Technology. 1 September 2024. Vol. 176, p. 111013. DOI 10.1016/j.optlastec.2024.111013.

Publikácia:

FEILER, Martin [65 %] - **ZIMAN, Martin** [15 %] - KOVÁČ, Jaroslav jr. [10 %] - KUZMA, Anton [5 %] - UHEREK, František [5 %]. Design of Optimal SPR-Based Multimode Waveguide Sensor for a Wide Range of Liquid Analytes. In *Photonics*. Vol. 10, iss. 6 (2023), Art. no. 618 [10] s. ISSN 2304-6732 (2021: 2.536 - IF, Q3 - JCR Best Q, 0.558 - SJR, Q2 - SJR Best Q). V databáze: DOI: 10.3390/photonics10060618 ; WOS: 001017896200001 ; CC: 001017896200001 ; SCOPUS: 2-s2.0-85163794308..

Citovaná v:

SHAHBAZ, Muhammad; BUTT, Muhammad A.; PIRAMIDOWICZ, Ryszard. A Concise Review of the Progress in Photonic Sensing Devices. In: *Photonics*. MDPI, 2023. p. 698.